



Defect engineering-mediated Co_9S_8 with unexpected catalytic selectivity for heterogeneous Fenton-like reaction: Unveiling the generation route of $^1\text{O}_2$ in V_S active site

Zhimo Fang^{a,b}, Juanjuan Qi^{a,*}, Wenxing Chen^c, Lin Zhang^a, Jianhui Wang^d, Caili Tian^d, Qin Dai^a, Wen Liu^e, Lidong Wang^{a,*}

^a Key Laboratory of Resources and Environmental System Optimization, Ministry of Education, College of Environmental Science and Engineering, North China Electric Power University, Beijing 102206, China

^b National Engineering Research Center of New Energy Power Generation, North China Electric Power University, Beijing 102206, China

^c Beijing Key Laboratory of Construction Tailorable Advanced Functional Materials and Green Applications, School of Materials Science and Engineering, Beijing Institute of Technology, Beijing 100081, China

^d Institute of Energy Resources, Hebei Academy of Sciences, Shijiazhuang 050081, China

^e Key Laboratory of Water and Sediment Sciences, Ministry of Education, College of Environmental Sciences and Engineering, Peking University, Beijing 100871, China

ARTICLE INFO

Keywords:

Sulfur vacancy
Generation mechanism
Singlet oxygen
Theoretical calculation
Electronic structure

ABSTRACT

Singlet oxygen ($^1\text{O}_2$) plays a crucial role in Fenton-like reactions due to its high efficiency and selectivity in removing trace organic pollutants from complex water matrices. Defect engineering, which allows the efficient exposure of active sites and optimization of electronic structures, has rapidly emerged as a fundamental strategy for enhancing $^1\text{O}_2$ yield. Herein, we introduce tunable sulfur vacancy (V_S) density into Co_9S_8 catalysts for peroxymonosulfate (PMS) activation. The modulation of the octahedral Co (CoS_6) and tetrahedral Co (CoS_4) electronic structures by V_S triggers the unexpected selective generation of $^1\text{O}_2$. The V_S /PMS system exhibits excellent resistance to interference and highly selective degradation of electron-donating organic pollutants. Experimental and theoretical calculations revealed a new evolutionary route for $^1\text{O}_2$ involving two phases (Phase I: $\text{HSO}_5^- \rightarrow ^*\text{O}$, Phase II: $^*\text{O} + \text{HSO}_5^- \rightarrow ^*\text{OO} \rightarrow ^1\text{O}_2$). This study provides a molecular-level understanding of V_S -mediated catalytic selectivity for high-efficient decontamination applications.

1. Introduction

Serious water pollution, including naturally occurring pollutants and man-made synthetic chemicals, exacerbated the freshwater crisis. In recent decades, advanced oxidation processes (AOPs) based on peroxymonosulfate (PMS) activation, specifically the Fenton-like reaction, have emerged as highly promising methods for the treatment of trace persistent pollutants in water [1,2]. However, the coexistence of a variety of pollutants with varying toxicities and structures often leads to high treatment costs and the ineffective elimination of target pollutants. Therefore, a water treatment method that efficiently and selectively degrades target pollutants with complex components is urgently required [3].

The effectiveness of removing refractory organic pollutants through PMS-AOPs depends on the generation of different reactive oxygen

species (ROS) during PMS activation, including hydroxyl radicals ($\bullet\text{OH}$), sulfate radicals ($\text{SO}_4^{\bullet-}$), singlet oxygen ($^1\text{O}_2$) and so on [4,5]. Among ROS, $^1\text{O}_2$ has gained considerable research attention as a promising candidate for treating refractory organic pollutants in the environment due to its mild oxidation ability to aromatic organic compounds (2.2 V vs. NHE), higher tolerance to water matrices (including being inert to the inorganic ions and have a wide pH tolerance), and relatively long lifetime (over an hour in the gas phase and 10^{-6} – 10^{-3} s in solution) [6]. With its unoccupied π^* orbital, $^1\text{O}_2$ can selectively oxidize unsaturated organics through electrophilic addition and electron abstraction reactions. Active chlorine species have similar characteristics to $^1\text{O}_2$, and have excellent denitrification function in wastewater compared to free radicals. Meanwhile, researchers are also committed to transforming ozone into $^1\text{O}_2$ in ozone-AOPs to enhance the treatment compatibility of real wastewater containing rich inorganic anions. Therefore, it is

* Corresponding authors.

E-mail addresses: qijuanjuan@ncepu.edu.cn (J. Qi), wld@ncepu.edu.cn (L. Wang).

<https://doi.org/10.1016/j.apcatb.2023.123084>

Received 7 March 2023; Received in revised form 1 June 2023; Accepted 7 July 2023

Available online 11 July 2023

0926-3373/© 2023 Elsevier B.V. All rights reserved.

necessary to selectively generate different types of ROS according to the characteristics of pollutants. At present, many studies have extended homogeneous reaction systems to heterogeneous reaction systems, in which many carbon materials (nitrogen-doped carbon nanosheets [7], carbon nanotubes [8], and so on) and transition metal-based catalysts (metal oxide [9], single-atom catalyst [10], and so on) can effectively activate PMS to $^1\text{O}_2$, but this process is often accompanied by the generation of $\bullet\text{OH}$ and $\text{SO}_4^{\bullet-}$. The current bottleneck is the poor selectivity of PMS conversion and the low quantitative yield of $^1\text{O}_2$. Therefore, there is an urgent need to rationally design highly active centers in catalysts to realize the efficient and directional conversion of PMS to $^1\text{O}_2$.

Cobalt sulfide has excellent conductivity, stability, and cost effectiveness, indicating its enormous potential for use in various catalytic applications including PMS activation [11]. Wang et al. prepared $\text{CoS}_x/\text{SiO}_2$ catalysts by leveraging the synergistic effect of cobalt and sulfur species to efficiently activate PMS for the degradation of sulfamethoxazole (SMX) [12]. However, the surface S^{2-} on catalyst can be oxidized to S^0 or SO_4^{2-} by Co^{3+} generated from the reaction between Co^{2+} and PMS, which will influence the catalyst stability [13]. PMS activation by cobalt sulfide mostly generates radical, although a few cases of $^1\text{O}_2$ -dominated catalysis have also been reported, selectivity of ROS generation is difficult to control [14]. Some studies have proposed that changes in the electronic structure affected the catalytic selectivity [6,15]. Defect engineering, which involves tailoring the atomic distribution and surface property of nanomaterials, is a promising approach to optimizing the electronic structure and overcoming the aforementioned challenges. [16,17]. Similar to oxygen vacancy, sulfur vacancy (V_S) in cobalt sulfide results in an abundance of coordinatively unsaturated sites [18], which also affect PMS adsorption and activation. Wang et al. reported that sulfur vacancy facilitated the regeneration low valent metals (Mo^{4+}) to decompose PMS into ROS, in which $^1\text{O}_2$ plays a key role in the removal of pollutants [19]. However, Hu's group proposed that only a small part of PMS is converted into $^1\text{O}_2$ by the electron-poor Co^{2+} areas surrounding the V_S , resulting in minimal contribution pollutant removal in the V_S /PMS system [20]. Therefore, the mechanism of V_S -mediated PMS activation to generate ROS is not yet clear, and the dependence between concentrations of V_S and kinds of ROS needs to be clarified.

In this study, we developed a straightforward strategy for synthesizing V_S -containing Co_9S_8 catalysts with mixed flexible coordination states (CoS_6 octahedral and CoS_4 tetrahedral). The fine optimization of V_S concentration in Co_9S_8 catalyst can realized tunable degradation mechanisms (free radicals-dominated mechanism evolved into $^1\text{O}_2$ -dominated mechanism) to enhanced the catalytic performance. The optimum V_S /PMS system can achieve rapidly degradation of sulfamethazine (SMT) with the rate constants as high as 0.631 min^{-1} , about 42 times of the perfect Co_9S_8 crystal, and anti-interference ability against anions, cations, and natural organic matter (NOM). Density functional theory (DFT) calculations revealed that the presence of V_S can effectively modulate the d-band center of Co in different coordination environments, thereby improving the selectivity of PMS activation and reducing the reaction energy barrier for the key O^* intermediate toward $^1\text{O}_2$ generation. Meanwhile, excellent activity of $^1\text{O}_2$ showed a highly selective degradation toward electron-rich pollutants. This study contributes to efforts at using V_S -mediated catalytic selectivity as obtained through molecular-level engineering for efficient and sustainable wastewater remediation.

2. Experimental procedures

2.1. Catalyst synthesis

All the chemicals were purchased commercially which were described in Text S1 in the Supporting Information (SI). Deionized water and ultra pure water was used in this study, and all chemicals were used

directly without further purification. The catalysts were prepared as follows: 0.58 g of $\text{Co}(\text{NO}_3)_2 \cdot 6\text{H}_2\text{O}$ was dissolved in 50 mL methanol, then 50 mL methanol solution containing 0.64 g 2-MIM was added to the above solution. After stirring quickly for 30 min and standing at room temperature for 24 h, ZIF-67 crystals were collected by centrifugation, washed by methanol four times, and dried in vacuum at 60°C for 12 h. 120 mg ZIF-67 particles were ultrasonically dispersed in 60 mL ethanol, followed by the addition of (120 mg, 180 mg, 240 mg, and 360 mg) thioacetamide (TAA). After stirring 30 min, the mixture was transferred into 100 mL Teflon-lined autoclave and kept at 120°C for 4 h. The precipitate was centrifuged, washed with deionized water and ethanol three times, and dried in vacuum at 60°C for 12 h. Finally, the dried product was calcined at 600°C for 2 h in the argon atmosphere. Regarding the amount of TAA used, the obtained samples were denoted as $\text{Co}_9\text{S}_8\text{-X}$ ($\text{X} = 1, 2, 3$, or 4). As a reference, the control sample Co_9S_8 with stoichiometric atomic ratio (denoted as Co_9S_8) was prepared using cobalt nitrate and thioacetamide as the sources under the same condition.

2.2. Catalyst characterization

The scanning electron microscopy (SEM) was carried out using Hitachi S-4800. The transmission electron microscopy (TEM) and the energy dispersive X-ray spectroscopy (EDX) elemental mappings were performed on JEM-2100 F. The X-ray absorption fine structure spectra data were collected at BL14W1 station in Shanghai Synchrotron Radiation Facility (SSRF, operated at 3.5 GeV with a maximum current of 250 mA), respectively. Detailed methods are provided in Text S2. X-ray diffraction (XRD) data were obtained by a Bruker D8 Advance with Cu K α radiation. Raman spectra was obtained using LabRam HR Evolution. Inductively Coupled Plasma Optical Emission Spectrometer (ICP-OES) was used AGILENT 725-ES. X-ray photoelectron spectroscopy (XPS) was acquired by thermo ESCALAB 250XI, which was detailed in Text S3. Electron paramagnetic resonance (EPR) was obtained by Bruker A300, which was used to obtain the information about vacancies concentration and the reactive oxygen species. The electrochemical properties of catalysts were analyzed by i-t current, Tafel polarization curves and electrochemical impedance spectrum (EIS) on an electrochemical workstation (CHI 760E) using carbon paper electrode coated with catalyst powder as the working electrodes, Pt electrode as counter electrode, calomel electrode as reference electrode. and 0.1 M Na_2SO_4 as the bath solution.

2.3. Experiment and methods

The degradation tests were carried out in a 150 mL conical flask at room temperature (25°C). 0.1 M NaOH and H_2SO_4 were used to adjust the initial pH of the solution containing PMS. Experiment details are provided in Text S4. Detection methods of organic pollutants, evaluate methods of degradation performance (the removal efficiency and reaction rate), detection methods of degradation intermediates, and detection methods of ROS are provided in Text S5, Analysis methods of intermediate toxicity are provided in Text S6. The calculation method of nucleophilicity index is provided in Text S7.

2.4. Calculations

Vasp. From first-principles, the projector augmented wave method was performed with the "Vienna ab initio simulation package" (VASP 5.4.1), and the Perdew-Burke-Ernzerh of exchange correlation functional was employed. The cutoff energy was set to 400 eV with a plane-wave basis to ensure accurate results. K points in the Brillouin zone were set to $2 \times 2 \times 1$ within the Gamma Scheme for structural optimization. The vacuum slab was set to 15 Å to avoid interaction error between neighboring supercells. The convergence thresholds of the energy and force were selected as 10^{-4} eV and 0.02 eV/Å in the calculation of

structural optimization. The climbing image nudged elastic band (NEB) method was utilized to locate the minimum energy pathways (MEPs) from an initial state (IS) to its final state, and the transition state (TS) was localized using the climbing image method and verified with a single imaginary frequency. For the PMS molecule adsorbed on catalyst the adsorption energy E_{ads} is defined as.

$$E_{\text{ads}} = E_{\text{PMS/catalyst}} - (E_{\text{PMS}} + E_{\text{catalyst}}) \quad (1)$$

where $E_{\text{PMS/catalyst}}$, E_{PMS} , and E_{catalyst} are the total energies of the PMS/catalyst system, the isolated PMS molecule, and catalyst in the same slab, respectively.

Gaussian. The calculation of HOMO and LOMO was optimized by Gaussian 16 based on DFT with the b3lyp/6–311 g (a, p) basis sets. The Fukui index was calculated by using Multiwfn software.

3. Results and discussion

3.1. Characterization and structure analysis

The synthesis process of Co_9S_8 hollow polyhedron was depicted in Fig. 1a. First, cobalt salts and 2-methylimidazole (2-MIM) were used as sacrificial templates in methanol to generate highly homogeneous ZIF-67 nanoparticles with a polyhedron morphology through room temperature precipitation [21]. Subsequently, the S ions released through TAA hydrolysis rapidly reacted with Co ions on the surface of ZIF-67 to form a thin sulfide layer. This sulfide layer acted as a physical barrier,

preventing direct contact and any chemical reaction between external S ions and internal Co ions. The Co and S ions must diffuse through this newly formed sulfide layer to continue the sulfidation reaction. A similar Kirkendall effect can explain the evolution inside the hollow structure in the solution [22,23]. In this process, the ZIF-67 precursor acted as a self-template for the formation of a hollow polyhedron shape. Finally, the hollow Co_9S_8 structure was obtained through calcination, yielding $\text{Co}_9\text{S}_8\text{-X}$. Scanning electron microscopy results revealed that $\text{Co}_9\text{S}_8\text{-3}$ had an orthododecahedral morphology (Fig. 1b). TEM characterization revealed that $\text{Co}_9\text{S}_8\text{-3}$ was a hollow dodecahedron with a diameter of approximately 400 nm (Fig. 1c-d). HRTEM image revealed that the lattice stripe spacings of Co_9S_8 (PDF#19-0364) were 0.17 nm (440) and 0.19 nm (511), respectively (Fig. 1e) [24]. The presence of V_{S} resulted in lattice disorder, which was clearly observed in the false-color image of the HRTEM image [25]. Additionally, elemental mapping images (Fig. 1f) confirmed the presence of Co and S elements in the $\text{Co}_9\text{S}_8\text{-3}$ sample. XRD was carried out to investigate the crystalline structure of as-prepared catalysts. The characteristic diffraction peaks of all the samples complied with cubic Co_9S_8 (PDF#19-0364), with no impurity and ZIF-67 residue (Fig. 1g). The Co_9S_8 samples exhibited diffraction peaks at $2\theta = 15.4, 29.9, 31.2, 35.7, 39.5, 47.4, 52.2$ and 54.3° , corresponding to the (111), (311), (222), (400), (311), (511), (440), and (531) crystal planes, respectively. The diffraction peak became wider and weaker in the $\text{Co}_9\text{S}_8\text{-X}$ samples as the TAA (thioacetamide) concentration increased, indicating a decrease in crystallinity and grain size [26]. The peak positions of the (440) plane in the $\text{Co}_9\text{S}_8\text{-X}$ samples slightly shifted to higher angles due to lattice shrinkage caused by the

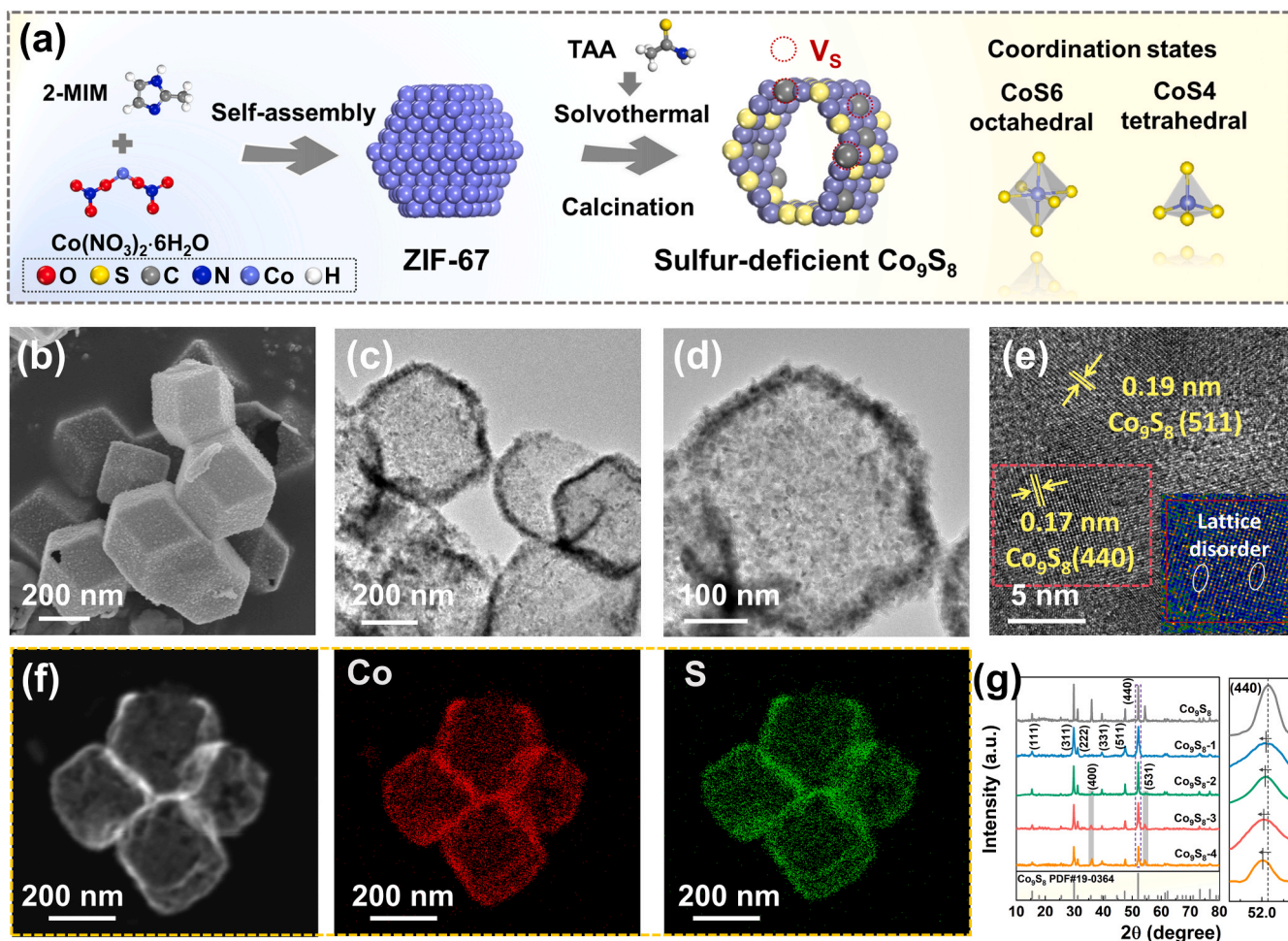


Fig. 1. (a) Schematic diagram of catalyst preparation process. (b) SEM image, (c-d) TEM image, (e) HRTEM image (insert: false-color image of the HRTEM image of the region outlined in red), (f) EDS elemental mapping image of $\text{Co}_9\text{S}_8\text{-3}$. (g) XRD patterns and magnified area of (440) peak of as-prepared catalysts.

existence of V_S [27]. Excessive TAA could be used as a reducing agent to reduce trivalent cobalt to divalent cobalt, while also adsorbing on the surface of primary nanocrystals, partially hindering crystal growth and leading to the formation of vacancy structures. Therefore, controlling the feed concentration of TAA during the solvothermal process can achieve adjustable sulfur vacancy concentration in the Co_9S_8 catalyst.

Raman spectroscopy was used to examine the molecular structure of the as-prepared catalysts. Fig. 2a illustrated that the five peaks located at 178.2, 451.9, 508.6, 599.5, and 659.2 cm^{-1} , attributed to the $F_{2g}^{(1)}$, E_{2g} , $F_{2g}^{(2)}$, $F_{2g}^{(3)}$, and A_{1g} typical Raman-active modes, respectively, for the cubic phase of Co_9S_8 [28]. Novelty, A_{1g} peaks of $\text{Co}_9\text{S}_8\text{-X}$ exhibited a continuous negative shift compared with that of Co_9S_8 , indicating the smaller short-range order [29]. Additionally, the intensity of $F_{2g}^{(1)}$ peaks decreased, attributed to the smaller long-range order [29]. The smaller long-range and short-range order in Co_9S_8 crystal indicated the existence of more V_S with increasing TAA concentration [30]. EPR spectra signal at $g = 2.003$ also verified the existence of V_S in the $\text{Co}_9\text{S}_8\text{-X}$ samples (Fig. 2b). The g value between 2.003 and 2.005 was related to V_S [31]. The results reflected that the V_S density increased with TAA concentration, which consistent with the Raman and XRD results that the V_S density reached the highest in $\text{Co}_9\text{S}_8\text{-4}$. The ICP-OES results yielded accurate atomic ratios of S and Co in the samples (Fig. 2c). The S/Co ratio of Co_9S_8 prepared using a stoichiometry precursor feed was 0.85, which was close to the ideal value of 0.89 for a perfect crystal, indicating that Co_9S_8 had no apparent defects. However, the S/Co ratio of $\text{Co}_9\text{S}_8\text{-X}$ initially decreased and then slightly increased with the increasing TAA concentration, indicating that the V_S density reached its peak in $\text{Co}_9\text{S}_8\text{-3}$ [29]. This finding was not in line with the results obtained from XRD and Raman analyses. We speculated that an excessively high V_S density might cause catalyst instability and lead to the loss of Co atoms.

XPS was conducted to analyze the surface elemental composition and corresponding electronic states of the samples. Fig. 2d exhibited that $\text{Co } 2p_{3/2}$ was further deconvoluted into three sub-peaks, associated with Co^{3+} (778.4 eV), Co^{2+} (780.8 eV), the satellite (784.9 eV) peaks [32, 33], respectively. Therefore, the loss of Co^{2+} will reduce the ratio of

$\text{Co}^{2+}/\text{Co}^{3+}$ in $\text{Co}_9\text{S}_8\text{-4}$. Fig. 2e demonstrated that the two characteristic peaks ($S 2p_{3/2}$ and $S 2p_{1/2}$) were located at 162.2 and 163.6 eV, respectively. The $S 2p_{3/2}$ peak was considered to the metal-S bond, and the $S 2p_{1/2}$ peak corresponded to a low-coordination S which was generally related to the V_S [34]. The relative atomic ratio of $\text{Co}^{2+}/\text{Co}^{3+}$ was calculated by the peak area ratio of $\text{Co}^{2+}/\text{Co}^{3+}$ in Co 2p spectra (Fig. 2f). The results showed that the relative ratios of $\text{Co}^{2+}/\text{Co}^{3+}$ were 1.32, 1.47, 1.67, 1.81, and 1.52, corresponding to Co_9S_8 , $\text{Co}_9\text{S}_8\text{-1}$, $\text{Co}_9\text{S}_8\text{-2}$, $\text{Co}_9\text{S}_8\text{-3}$, and $\text{Co}_9\text{S}_8\text{-4}$, respectively. The loss of Co^{2+} was more preferentially than Co^{3+} in thermodynamics [35]. The relative ratio of $S 2p_{1/2}/S 2p_{3/2}$ in $\text{Co}_9\text{S}_8\text{-4}$ sample was the highest (Fig. 2f). Noticeably, the binding energies of S 2p in $\text{Co}_9\text{S}_8\text{-X}$ were higher than that in Co_9S_8 because positively charged V_S would reduce the electron density on the catalyst surface [36]. As expected, the V_S density increased with an increase in the TAA concentration and reached the highest in $\text{Co}_9\text{S}_8\text{-4}$. Based on the preceding characterization analysis, V_S -rich Co_9S_8 catalysts were successfully prepared, in which the density of V_S could be regulated by changing the concentration of TAA.

The atomic local structure of the $\text{Co}_9\text{S}_8\text{-3}$ was further confirmed by X-ray absorption fine structure (XAFS) measurement, an elemental sensitive technique. In Fig. 3a, the normalized X-ray absorption near-edge structure (XANES) curves of Co K-edge revealed that the absorption edge of the $\text{Co}_9\text{S}_8\text{-3}$ was lower-energy shifted than that of Co_9S_8 , suggesting that the average oxidation state of Co in the $\text{Co}_9\text{S}_8\text{-3}$ was more negative, mainly due to the larger relative ratio of $\text{Co}^{2+}/\text{Co}^{3+}$, derived from existence of V_S . The Fourier transform (FT) extended X-ray absorption fine structure (EXAFS) (Fig. 3b) of the $\text{Co}_9\text{S}_8\text{-3}$ possessed only one main peak located at 1.69 Å, which was assigned to Co-S coordination. As we can see, the distance was shorter than that of Co_9S_8 (1.76 Å), revealing the possible shrinking of Co-S bonds. Quantitative EXAFS analysis was also performed. The EXAFS fitting curves of the $\text{Co}_9\text{S}_8\text{-3}$ were displayed in Fig. 3c. The local structural parameters of the $\text{Co}_9\text{S}_8\text{-3}$ were listed in Table S1. The EXAFS fitting results indicated that the 1st-shell (anchored by S atoms) averaged coordination number of the central atom Co was 3.4 (smaller to that of Co_9S_8 reference), with the bond length of 2.28 Å.

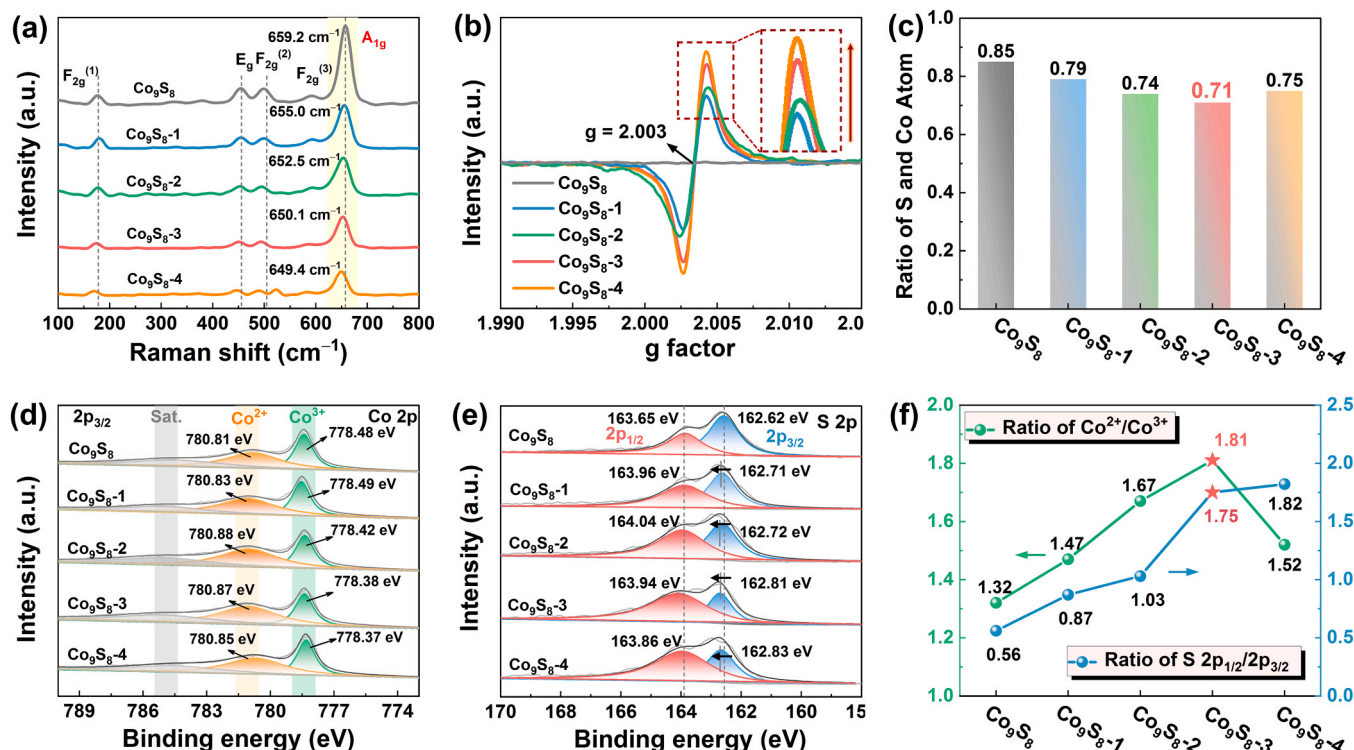


Fig. 2. (a) EPR spectra, (b) Raman spectra, (c) ICP-OES, (d) Co 2p XPS spectra, (e) S 2p XPS spectra of as-prepared catalysts. (f) The relative atomic ratio.

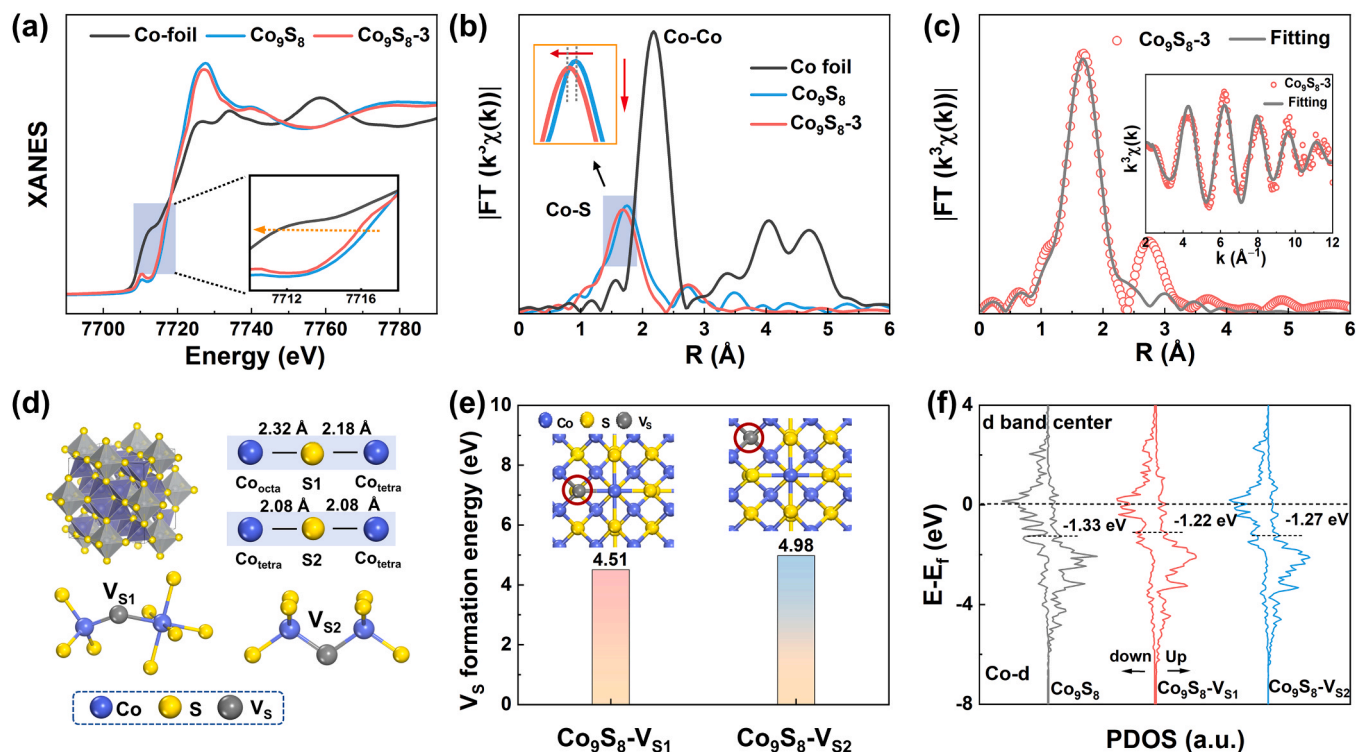


Fig. 3. (a) Normalized Co K-edge XANES and (b) Fourier transform of Co K-edge EXAFS spectra of Co₉S₈-3 and reference samples. (c) The EXAFS fitting curves of the Co₉S₈-3. Schematic representation of (d) Co₉S₈ original cell and the length of Co_{octa}-S1, Co_{tetra}-S1, and Co_{tetra}-S2. (e) The vacancy formation energy. (f) PDOS of Co₉S₈ (100) with no vacancy, Co₉S₈ (100) with V_{S1}, and Co₉S₈ (100) with V_{S2}.

To investigate the effect of defect engineering on Co₉S₈, DFT calculations were applied to explore the electronic structures of Co₉S₈. The original cell of Co₉S₈ contained CoS₄ tetrahedral (Co_{tetra}) and CoS₆ octahedral (Co_{octa}) (Fig. 3d). CoS₆ had a symmetric Oh structure, CoS₄ had a locally C_{3v} symmetric triangular distortion with one short and three longer Co-S distances. Two nonequivalent sulfur sites (S1 and S2) were either shared by Co_{octa} and Co_{tetra}, with a calculated bond length of 2.32 Å for Co_{octa}-S1 and 2.18 Å for Co_{tetra}-S1, and shared only by Co_{tetra} with a bond length of 2.08 Å Co_{tetra}-S2. Therefore, two non-equivalent V_S (V_{S1} and V_{S2}) might be formed, and their formation energies were calculated to be 4.51 and 4.98 eV, respectively (Fig. 3e), indicating that V_{S1} was easier to form than V_{S2} [37]. Moreover, the density of states (DOS) for Co₉S₈ (100) in the absence or presence of V_{S1}/V_{S2} was calculated. Fig. S1 showed that all the DOS passed through E_F, indicating Co₉S₈, Co₉S₈-V_{S1}, and Co₉S₈-V_{S2} exhibited metallic properties in terms of conductivity. The DOS of Co₉S₈-V_{S1}, and Co₉S₈-V_{S2} at Fermi level increased obviously compared to Co₉S₈, indicating that V_S played a crucial role in enhancing the conductivity. As shown in Fig. 3f, the d-band center energy (E_d) levels of Co₉S₈, Co₉S₈-V_{S1}, and Co₉S₈-V_{S2} with respect to E_F were 1.33, 1.22, and 1.27 eV, respectively. V_{S1} and V_{S2} exerted different effects on E_d, and the upward movement of E_d potentially affected the adsorption between the Co site and PMS. Based on these findings, we inferred that the presence of V_S has a regulatory effect on the electronic structure of catalysts, and the coordination structure influences this regulation ability.

3.2. Regulation of V_S for PMS activation

The catalytic performance of V_S regulation for PMS activation to remove SMT was evaluated. The concentration of SMT was determined using HPLC (Table S2). The SMT removal efficiency was negligible when Co₉S₈-X was used as an adsorbent, indicating the vital role of PMS activation (Fig. S2a). Fig. 4a displayed that PMS had minimal ability to remove SMT. However, the V_S-rich Co₉S₈-X catalysts exhibited good

catalytic activity, with the Co₉S₈-3/PMS system exhibiting the highest SMT degradation rate (pseudo-first-order kinetics (k_1) = 0.631 min⁻¹), almost 42 times higher than that of Co₉S₈ with no V_S (Fig. 4b). This fully proved that the constructed unsaturated defect states could indeed improve the catalytic activity, and V_S might dominate the PMS activation. The slight decline in activity of Co₉S₈-4 might be attributed to the loss of Co²⁺ sites. Co₉S₈-3 was selected for subsequent research owing to its excellent catalytic performance. The optimal concentrations of PMS (0.6 mM) and Co₉S₈-3 (150 mg·L⁻¹) were determined (Fig. S2b and S2c). A comparison of the amount of PMS consumed under the catalyst system of PMS alone, Co₉S₈/PMS, and Co₉S₈-3/PMS revealed that the PMS utilization of Co₉S₈-3 was significantly higher than that of the rest of the systems (Fig. 4c). Fig. 4d and S3, indicated the effect of the initial pH values (2.9–10.6 ± 0.2) on SMT removal. The removal efficiency of SMT under neutral and alkaline conditions exceeded 98 % within 10 min and was partly inhibited under acidic conditions, which was attributed to the leaching behavior of the Co element in acid media [38]. The changes in pH value were monitored during the SMT degradation in the initial pH value from 2.9 ± 0.2 to 10.6 ± 0.2 (Fig. S4a), which was detailed in Text S8. Meanwhile, pH buffer was used to maintain the pH value of SMT degradation (Fig. S4b), indicating that the addition of pH buffer had no effect on the experimental results.

To further evaluate the universal applicability of the catalyst, the influences of anions, cations and NOM on SMT removal were considered. Figs. 4d, S5a and S5b depicted that when Cl⁻ concentration increased from 0 to 20 mM, k_1 dramatically increased from 0.631 to 0.842 min⁻¹, and the decomposition rate of PMS rose from 67.5 % to 76.8 %. Therefore, it was inferred that the reason for the increase of k_1 might be attributed to the further decomposition of PMS by Cl⁻ to generate ¹O₂ according to Eqs. (1–3) [39–41], thus accelerating the SMT degradation. HCO₃⁻ and HPO₄²⁻ with concentration of 10 mM and a typical NOM (humic acid, HA) with concentration of 10 mg·L⁻¹ could hardly influence the SMT removal. However, the degradation rate decreased significantly when the concentration of HA was increased to

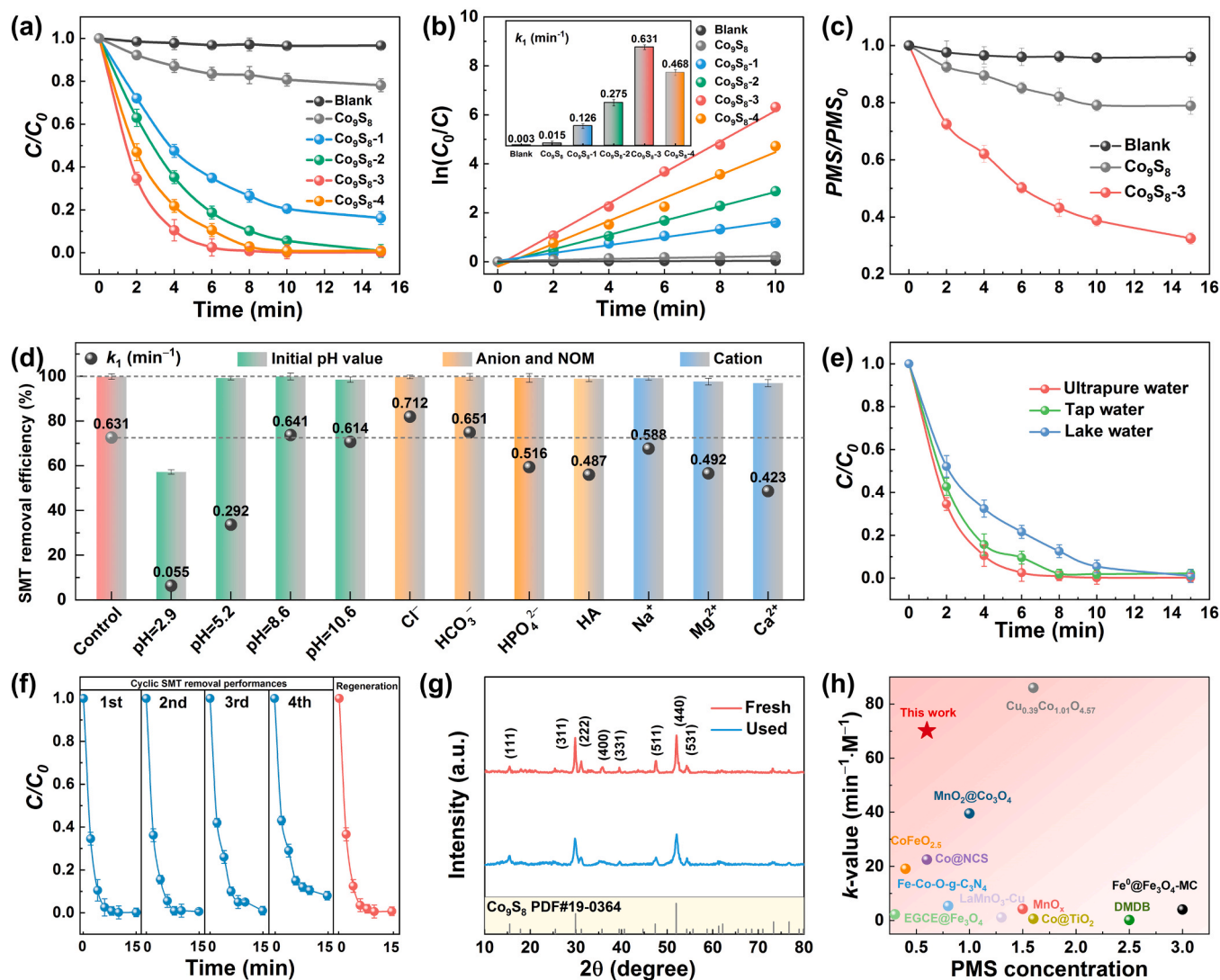
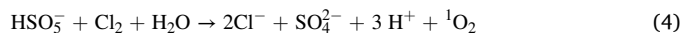


Fig. 4. (a) Degradation curves of SMT and (b) the corresponding pseudo first-order model (inset: the reaction rate constant) with a series of Co₉S₈. (c) The PMS decomposition rates. (d) The effect of the initial pH value, anions, NOM, cations, and (e) water qualities within 15 min on the SMT degradation in the Co₉S₈-3/PMS system. (f) The cyclic SMT removal performances of Co₉S₈-3/PMS systems. (g) XRD patterns of fresh and used Co₉S₈-3. (h) Comparison of pollutant removal efficiency and time between Co₉S₈-3 and other recently reported catalysts. Reaction condition: [catalyst] = 150 mg·L⁻¹, [PMS] = 0.6 mM, [SMT] = 10 mg·L⁻¹, [anions, cations] = 10 mM, [HA] = 10 mg·L⁻¹, and initial pH= 6.9 ± 0.2.

about 220 mg·L⁻¹ (1 mM), as shown in Fig. S6, which was much higher than the concentration of natural organic matter in the real water [42]. The above phenomenon might be attributed to the competition adsorption between HA and PMS for the active sites of Co₉S₈-3 [43]. Figs. 4d and S7 showed that the presence of cations inhibited the reaction to varying degrees, and the rate constants for SMT degradation followed the order: Na⁺ > Mg²⁺ > Ca²⁺. Cations competed with Co ions to get adsorbed on the catalyst surface in order to reduce the available active sites on the surface. The introduction of cations would thus lead to an increase in the ionic strength of catalyst agglomeration, and Na⁺ exerted the lowest inhibition due to its low voltage electric bilayer effect and low ion exchange capacity [44]. Fig. 4e, showed that the rate constant decreased slightly and the removal efficiency still reached 90 % within 15 min in different water qualities, including tap water and lake water (water sample from Cuiming Lake in Beijing), attributed to the possible presence of inorganic ions and organics competing with target pollutants for active ROS [45]. The Co₉S₈-3/PMS system could achieve the 45.3 % of the real mineralization rate within 2 h (Fig. S8). The amount of CO₂ generation within 2 h was detected to further prove that organic mineralization exists in the system, detailed in Text S9. The

Co₉S₈/PMS system could achieve a mineralization rate of 32.1 %, lower than that in the Co₉S₈-3/PMS system, which might be attributed to the limited ability of the catalyst to activate PMS, resulting in less generation of ROS with excellent indiscriminate removal ability.



The catalyst unfolded superior stability in cyclic SMT degradation, reaching 95 % removal within 15 min of the first three cycles (Fig. 4f). Although the SMT removal rate decreased to 92 % in the fourth cycle, the crystal structure and electronic state of Co₉S₈-3 did not significantly change after the cyclic reaction (Figs. 4g, S9, and S10). The XPS analysis of both fresh and used Co₉S₈-3 indicated a favorable oxidation-reduction process of Co²⁺–Co³⁺–Co²⁺ on the V_S-rich Co₉S₈-3 surface during PMS activation. The decrease in S 2p_{1/2} peak area indicated the participation of V_S in the reaction. The fairly low Co leaching concentration (≤ 0.15 mg·L⁻¹) was shown in Co₉S₈-3/PMS system, which was much lower than the permissible limit (1 mg·L⁻¹) given by

the Chinese National Standard (GB 25467–2010). These results showed that the Co₉S₈-3 catalyst had good stability. The homogeneous catalytic system constructed by adding the same amount of leached metal ions or directly using the leaching solution (without catalyst) exhibited negligible SMT degradation (Fig. S11), which confirmed the dominance of heterogeneous catalysis in the Co₉S₈-3/PMS system. Due to the high chemical stability of Co₉S₈-3, the slight decrease in its activity during cyclic SMT degradation might be attributable to the accumulation of oxidative intermediates on the surface of the catalyst [46]. However, these aromatic intermediates could be easily removed, and the catalyst's activity could be fully restored through chemical elution (with ethanol for 1 h). In addition, due to the abundance of V_S, Co₉S₈-3 exhibited remarkable PMS activation activity, achieving high-speed SAs degradation with a higher k_1 -value of 70.11 min⁻¹ M⁻¹ at lower PMS concentrations compared with most catalysts and had a wide pH adaptability (Fig. 4h and Table S3). Overall, the use of the Co₉S₈-3/PMS system in sewage remediation is practically feasible. The response surface method (RSM) was used to find the optimal process conditions (Fig. S12, Table S4, and Table S5), which were as follows: catalyst dosage of 300 mg·L⁻¹, PMS concentration of 0.83 mM, pH value of 10.1, and the predicted reaction rate was $k_1 = 1.086$ min⁻¹. The process conditions was detailed in Text S10. These results could guide the design of Co₉S₈-3/PMS processes in sewage remediation.

3.3. Identification of reactive oxygen species

The PMS activation process generally involves ROS production,

which was appraised by the EPR technique and the quenching experiments. When 5,5-dimethyl-1-pyrroline N-oxide (DMPO) and 2,2,6,6-tetramethyl-4-piperidino (TEMP) were used as the spin-trapped reagent, no EPR signal was detected in PMS alone system (Fig. S13). In the absence of V_S system (Co₉S₈/PMS system), only the signal of DMPO-•OH/SO₄^{•-} adducts was found. However, with an increase in V_S density, the signal of the DMPO-•OH/SO₄^{•-} adducts began to disappear in the Co₉S₈-2 sample (Fig. 5a). The strength of the triplet TEMP-¹O₂ signal significantly increased with an increase in V_S content but slightly decreased in the Co₉S₈-4/PMS system (Fig. 5b). These results indicated that V_S might mediate the generation of ¹O₂. However, excessive V_S could lead to a decrease in TEMP-¹O₂ intensity in the Co₉S₈-4/PMS system, resulting in a slower reaction rate. Moreover, excessive V_S can impede the internal and interfacial migration of charge carriers due to poor crystallinity [47,48], as indicated by findings from electrochemical impedance spectroscopy (EIS), Tafel polarization curves and the amperometric $i - t$ test. Fig. 5c illustrated that the arc radius initially decreased and then increased with an increase in vacancy concentration, indicating an excess of vacancies was conducive to improving charge transfer resistance of catalyst [49]. As indicated in Fig. 5d, the corrosion current of Co₉S₈-3 was 0.762 mA, higher than those of Co₉S₈ (0.105 mA), Co₉S₈-1 (0.308 mA), Co₉S₈-2 (0.423 mA), and Co₉S₈-4 (0.727 mA), indicating the excellent electron transfer performance of Co₉S₈-3 [50]. The results indicated that excessive V_S would hinder carriers' internal and interface migration, resulting in the decline of the electron transfer ability of the catalyst. The amperometric $i - t$ test was a measure to reveal the electron transfer during PMS activation and

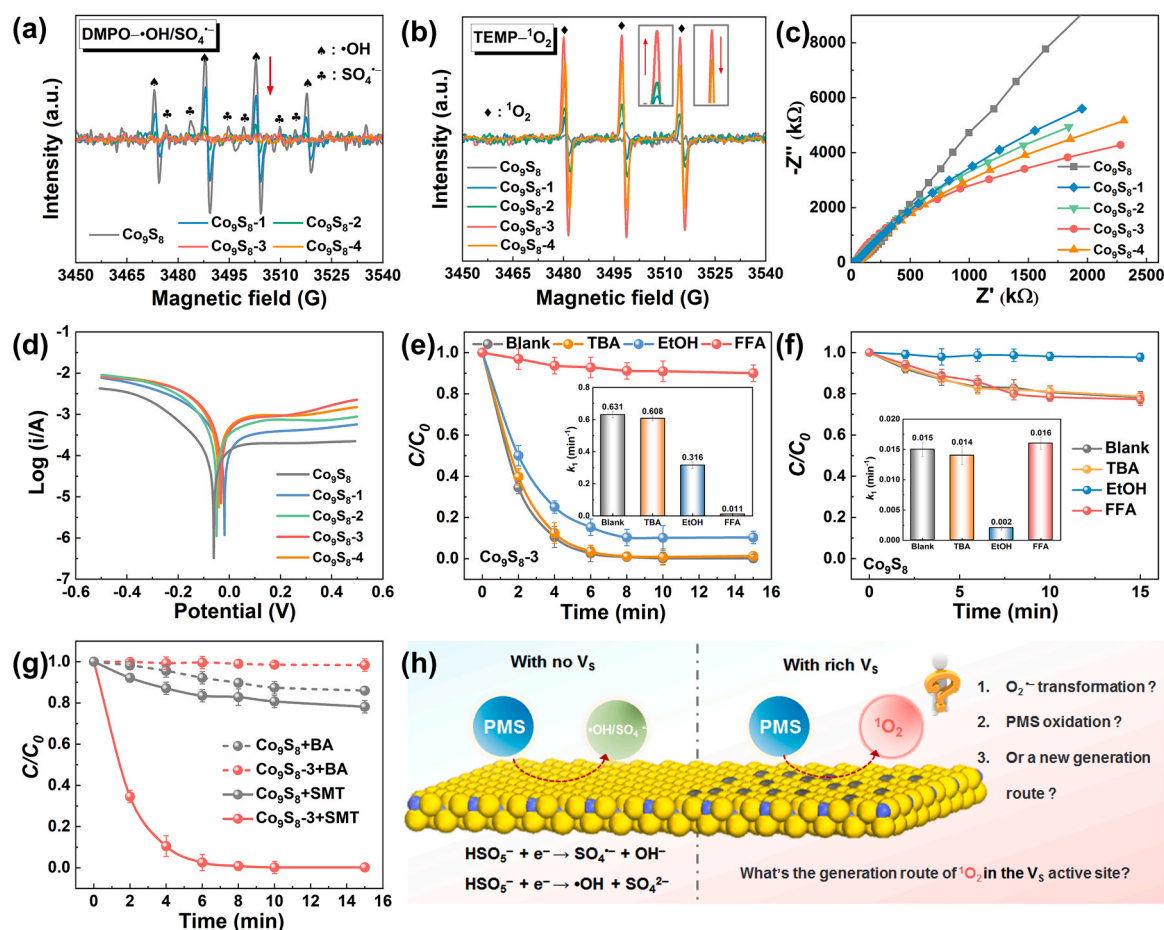


Fig. 5. (a) EPR spectra of •OH and SO₄^{•-} (3 min). (b) EPR spectra of ¹O₂ (3 min). (c) EIS. (d) Tafel polarization curves. (e) The quenching experiments in Co₉S₈-3/PMS system (inset: degradation rates (k_1 values) of SMT). (f) The quenching experiments in Co₉S₈/PMS system (inset: degradation rates (k_1 values) of SMT). (g) Degradation curves of BA. (h) Radical and non-radical generation route in Co₉S₈ with and without V_S. Reaction condition: [catalyst] = 150 mg·L⁻¹, [PMS] = 0.6 mM, [SMT] = 10 mg·L⁻¹, [BA] = 10 mg·L⁻¹, [TBA, EtOH] = 150 mM, [FFA] = 10 mM, and initial pH= 6.9 ± 0.2.

pollutant degradation. Fig. S14 presented that the current increased in varying degrees after PMS addition, with the most evident increase observed in Co₉S₈-3, indicating that the number of electron transfers between Co₉S₈-3 and PMS was maximal, consistent with the EPR and experimental results. The current randomly decreased after SMT was added, and the current change was not significant compared with that observed after PMS addition. This suggested that SMT provided electrons to the catalyst, but the effect was not significant [51].

Quenching experiments were further conducted to identify the types of ROS in the different Co₉S₈-3/PMS systems. Tertbutyl alcohol (TBA) was used as the •OH scavenger, ethanol (EtOH) was used as the •OH and SO₄^{•−} scavenger, and furfuryl alcohol (FFA) was used as the ¹O₂ scavenger [12,38,52]. Fig. 5e inferred that ¹O₂ predominated, followed by SO₄^{•−} played little role in Co₉S₈-3 catalysts, which was inconsistent with EPR results. The introduction of TBA presents no effect on SMT removal, ruling out the role of •OH. Significantly, FFA might interact with PMS to amplify the function of ¹O₂. However, the decomposition rate of PMS remained almost unchanged in the systems of Co₉S₈-3/PMS/FFA and Co₉S₈-3/PMS (Fig. S15a), which indicated that PMS might preferentially react with the active site on the surface of Co₉S₈-3 catalyst to generate ¹O₂ and was not consumed by FFA. L-histidine was used as the quencher of ¹O₂, and the inhibition result was similar to that of FFA (Fig. S15b) [53], further proving the dominant role of ¹O₂. Fig. 5f indicated that SO₄^{•−} alone participate in the degradation of SMT in the Co₉S₈/PMS system. In order to more accurately judge whether SO₄^{•−} play a role in Co₉S₈-3/PMS system, benzoic acid (BA) was used as the target pollutant, which can only be removed by free radicals. The results showed that BA was hardly degraded in Co₉S₈-3/PMS system, while the results were opposite in Co₉S₈/PMS system (Fig. 5g). The service life of ¹O₂ in D₂O was significantly prolonged (~4.2 μs in H₂O vs ~55 μs in D₂O) [5]. Fig. S16 indicated that the SMT removal rate in Co₉S₈/PMS system had almost no change adding D₂O instead of water as the reaction solvent. However, the SMT removal rate in the Co₉S₈-3/PMS system was slightly enhanced. Therefore, we inferred that ¹O₂ is absolutely dominant for removing SMT in the rich V_s system (Fig. 5h). Studies have demonstrated that O₂^{•−} radicals might act as intermediates that generate ¹O₂ through metal-mediated PMS activation [54,55]. p-BQ was used to verify the effect of O₂^{•−}, indicating that p-BQ had little effect on Co₉S₈-3/PMS system (Fig. S17). In addition, the result of the N₂ bubbling experiment confirmed that dissolved oxygen had little effect on SMT degradation (Fig. S18a) [2], and the strength of the TEMP-¹O₂ signal almost remains basically unchanged in the N₂ atmosphere (Fig. S18b), so it was confirmed that ¹O₂ was not generated by further evolution of dissolved oxygen. Altogether, what is the generation route of ¹O₂ in the V_s active site?

3.4. Theoretical study on PMS activation kinetics

DFT calculations were analyzed the activation process of PMS to discuss its theoretical activity trend and to determine its correlation with the experimental results [56]. The adsorption energy (*E*_{ads}) and the O-O bond length (*l*_{O-O}) predicted the superior activation site of PMS in Co₉S₈ with no vacancy and V_s (Fig. S19). The results showed that PMS tended to adsorb on the Co_{octa} site in Co_{octa}-V_{S1}-Co_{tetra} and Co_{tetra} site in Co_{tetra}-V_{S1}-Co_{tetra}. The *l*_{O-O} is crucial in judging the activation of PMS, which could be broke to generate ROS. The results showed that the *l*_{O-O} adsorbed on the Co_{octa} site in Co_{octa}-V_{S1}-Co_{tetra} and Co_{tetra} site in Co_{tetra}-V_{S1}-Co_{tetra} were relatively significant change relative to the initial PMS [57]. Meanwhile, the pathways of PMS selective conversion to •OH, SO₄^{•−}, and ¹O₂ on different sites were further discussed by the transition state (TS) search method. Fig. S20 indicated that the corresponding reaction energy barriers (*E*_b) of Co₉S₈ was 0.75 eV which was lower than Co₉S₈-V_{S1} and Co₉S₈-V_{S2} (1.24 and 0.97 eV). The critical *E*_b of 0.9 eV would determine whether chemical reactions could occur at room temperature [58]. Therefore, HSO₅[−] on Co₉S₈ could undergo the break of O-O bond to generate SO₄^{•−} and •OH free radicals rather than Co₉S₈-V_{S1}

and Co₉S₈-V_{S2}, which was consistent with the experimental result. Therefore, two reaction intermediates for ¹O₂ generation at V_s-rich sites were emphatically studied based on the new insight into the ¹O₂ generation mechanism. The first pathway was the loss of the H atom to generate •SO₅[−], and then the rapid reaction of •SO₅[−] to generate ¹O₂, SO₄^{2−} and S₂O₈^{2−} [14]. Another pathway was to lose HSO₄[−] to produce the surface active oxygen (*O) and then react with HSO₅[−] to generate ¹O₂ [4]. Fig. 6a showed that the energy of generating SO₅[•] at different sites slightly increased which was more difficult than generating *O. TEMP was used to capture ¹O₂ in the methanol system to eliminate the possibility that oxygen might come from H₂O. The peak intensity of TEMP-¹O₂ decreased slightly (Fig. S21a), indicating that oxygen in H₂O had almost no effect on the ¹O₂ production. In-situ Raman spectroscopy was used to monitor the process of catalyst activation of PMS, which was detailed in Text S11. Fig. S21b indicated that a weak peak appeared at 1020 cm^{−1} only in the Co₉S₈-3/PMS system, attributing to surface oxygen atoms (O*) produced by the reaction between Co₉S₈-3 and PMS, which was consistent with DFT results.

The optimal pathway for the generation of ¹O₂ in the presence of V_s is presented in Figs. 6b and 6c. Figs. 6d and 6e present the relative energy for ¹O₂ generation and the different selectivity of V_{S1} and V_{S2}. The generation of ¹O₂ comprised two phases. In the phase I (HSO₅[−] → *HSO₅[−] → *O + *HSO₄[−] → *O + HSO₄[−]), HSO₅[−] was adsorbed on the catalyst surface and the O-O bond was broken to generate *O and HSO₄[−]. In the phase II (*O + HSO₅[−] → *O + *HSO₅[−] → 2 *O + *HSO₄[−] → ¹O₂ + HSO₄[−]), *O further reacted with the adsorbed HSO₅[−] to generate ¹O₂ and HSO₄[−]. The ¹O₂ intermediate (*O) optimized the d-band electronic structure of Co_{octa} in Co₉S₈-V_{S1}, making the *E*_d closer to the *E*_f (1.12 eV) than that for Co₉S₈-V_{S2} (1.21 eV). This optimized structure of Co₉S₈-V_{S1} accelerated the reaction between HSO₅[−] and O* in phase II. The *E*_b values of Co₉S₈-V_{S1} (0.31 and 0.45 eV) for the formation of *O-OHSO₅[−] (TS) in phase I and *OO-OHSO₃[−] (TS) in phase II were lower than that of Co₉S₈-V_{S2} (0.87 and 0.46 eV; Fig. 6f), which was highly beneficial for the decomposition of HSO₅[−]. The adsorption of HSO₅[−] on Co₉S₈-V_{S1} to and the resolution of HSO₄[−] and ¹O₂ were more favorable than with Co₉S₈-V_{S2} owing to the different effects of the two nonequivalent V_s on the local electronic state (Figs. 6g and 6h) [59]. Furthermore, V_{S1} was verified to have the largest contribution to the production of ¹O₂. The adjusted *E*_d of the Co₉S₈-V_{S1} surface enhanced the O-O bond fracture kinetics, resulting in the lowest reaction energy barrier and superior PMS activation performance [60]. The aforementioned results indicated that the catalysts with and without V_s exhibited different electronic structures of metal atoms, *E*_d positions, and adsorption capacities for intermediates, which might ultimately affect the ROS selectivity.

3.5. Determination of possible degradation pathways

The Fukui index based on DFT using Multiwfn software revealed the most vulnerable sites of SMT [8,61]. Fig. 7a was the SMT molecular. As electrophilic ROS, ¹O₂ would attack the sites being prone to electron loss mainly located on the benzene ring and -NH-SO₂- bond in SMT molecules in Fig. 7b (the HOMO of SMT). Fig. 7c indicated the charge distribution and Fukui index (radical (*f*⁰) and electrophilic (*f*[−])) of each atom in SMT, where atoms with the higher *f*[−] value were more vulnerable to ¹O₂ attacks, and higher *f*⁰ value could indicate the regioselectivity of radical species (•OH and SO₄^{•−}). The results indicated that C4, N8, C13, C16, C18, and N23 atoms were the preferred sites to be attacked by ¹O₂. The value of *f*⁰ showed that the free radical attack region moved to the substituent of the six-membered ring, mainly at N6 and C5. Combined with the oxidation products determined by HPLC-mass spectrometry (HPLC-MS) in Tables S6 and S7, the possible three degradation pathways of SMT were suggested in Fig. 7d and Fig. S22 [62,63]. The •OH and SO₄^{•−} radicals could react with organic compound via single-electron transfer, radical adduct formation, and hydrogen abstraction, and ¹O₂ could react with organic compound via single-electron transfer and electrophilic addition. Due to the slightly

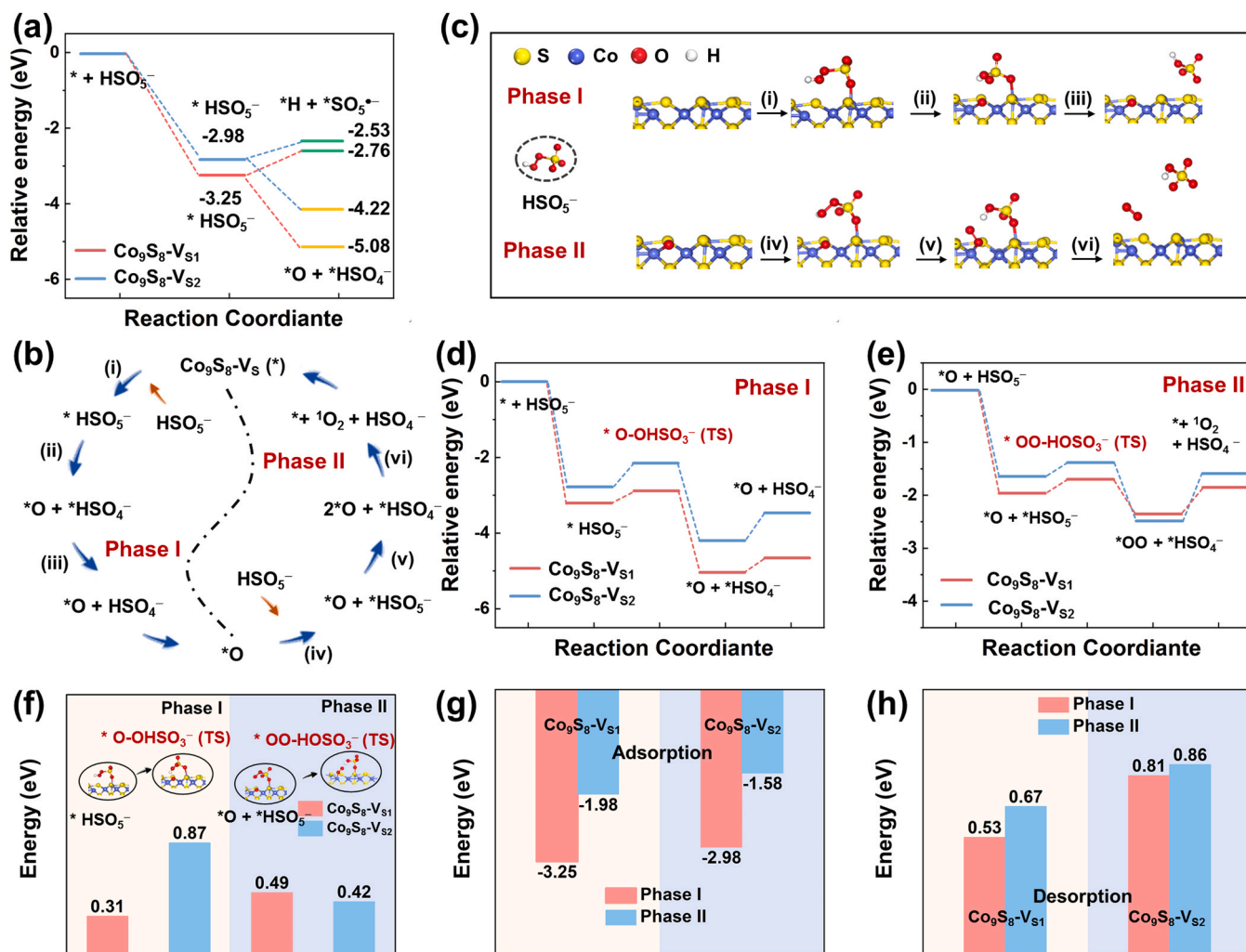


Fig. 6. (a) The potential energy for PMS decomposition to two key reaction intermediates. (b) and (c) Proposed reaction process for $^1\text{O}_2$ generation. (d) and (e) Calculated energy by two substances for the PMS to $^1\text{O}_2$ process. (f) The energy for forming TS. (g) The adsorption of PMS and (h) desorption of HSO_4^- and $^1\text{O}_2$. The adsorption site on the catalyst is denoted by an asterisk (*). The purple, yellow, red, and white atoms are Co, S, O, and H.

different attack sites and reaction mechanism, the degradation pathways of free radical- and $^1\text{O}_2$ -dominated systems were slightly different. The degradation path in the free radical-dominated system was explicitly described in Text S12.

In the $^1\text{O}_2$ -dominated system $^1\text{O}_2$ could react with organic compound via single-electron transfer and electrophilic addition [64]. In pathway I, P2 (m/z 158) and P4 (m/z 124) was formed by the single-electron transfer of $^1\text{O}_2$ attacking N8 atoms, resulting in S-N bond cleavage [63], which was matched with higher f^- of N8 (0.0560). P2 was directly oxidized by $^1\text{O}_2$ to generate P3 (m/z 124). P4 underwent cycloaddition via electrophilic addition to generated P5 (m/z 154). P5 could further form carbonyl compounds and C-N broke due to single-electron transfer reaction to generate P6 (m/z 124), which was a unique attack pathway in the $^1\text{O}_2$ -dominated degradation system [65]. Meanwhile, P5 underwent the processes of open ring and C-N bond cleavage to generate P7 (m/z 100) and P8 (m/z 59). In pathway II, SMT could be directly oxidized through the attack of N23 atom via $^1\text{O}_2$ pathway to generate the products P9 and P10 [66], which was matched with higher f^- of N23 (0.1041). The products were the same as free radical pathway products, but the reaction method was slightly different. In pathway III, SMT underwent smile rearrangement to generate products P11 (m/z 244) and P12 (m/z 242), which are initiated by was initiated by an aniline radical cation of SMT via an electron transfer mechanism [67].

Some products were the same due to the single electron transfer

reaction in the free radical and $^1\text{O}_2$ -dominated system. Some of the same products might come from different reactions, such as radical pathway III and $^1\text{O}_2$ pathway II. Due to the unique electrophilic addition reaction of $^1\text{O}_2$, adducts and carbonyl containing compounds (P5 and P6) were generated. Meanwhile, both systems could break chemical bonds to generate small molecules by the single electron transfer reaction, which further proved that the TOC mineralization process exists in the $^1\text{O}_2$ -dominated system. In addition, the ECOSAR software was used to evaluate the acute and chronic toxicity of SMT and its intermediates [68], and the specific values were shown in Table S6, which was detailed in Text S13. The values were visualized to show the toxicity level of fish, daphnid, and green algae more intuitively. Fig. 7e indicated that the toxicity of most intermediates was lower than that of SMT, but some intermediates were still very toxic in the degradation process. Therefore, it was necessary to pay attention to the potential risks caused by some intermediates of SMT.

3.6. Performance of $\text{Co}_9\text{S}_8\text{-3}$ for practical decontamination application

The practical applicability of the $\text{Co}_9\text{S}_8\text{-3}$ /PMS system and the selective degradation ability of $^1\text{O}_2$ for various pollutants (namely aniline (ANI), sulfanilamide (SA), SMT, sulfamerazine (SMR), sulfamethoxazole (SMX), sulfathiazole (STZ), phenol (Ph), bisphenol A (BPA), nitrobenzene (NB), and BA) with electron-donating ($-\text{NH}_2$ and $-\text{OH}$) and

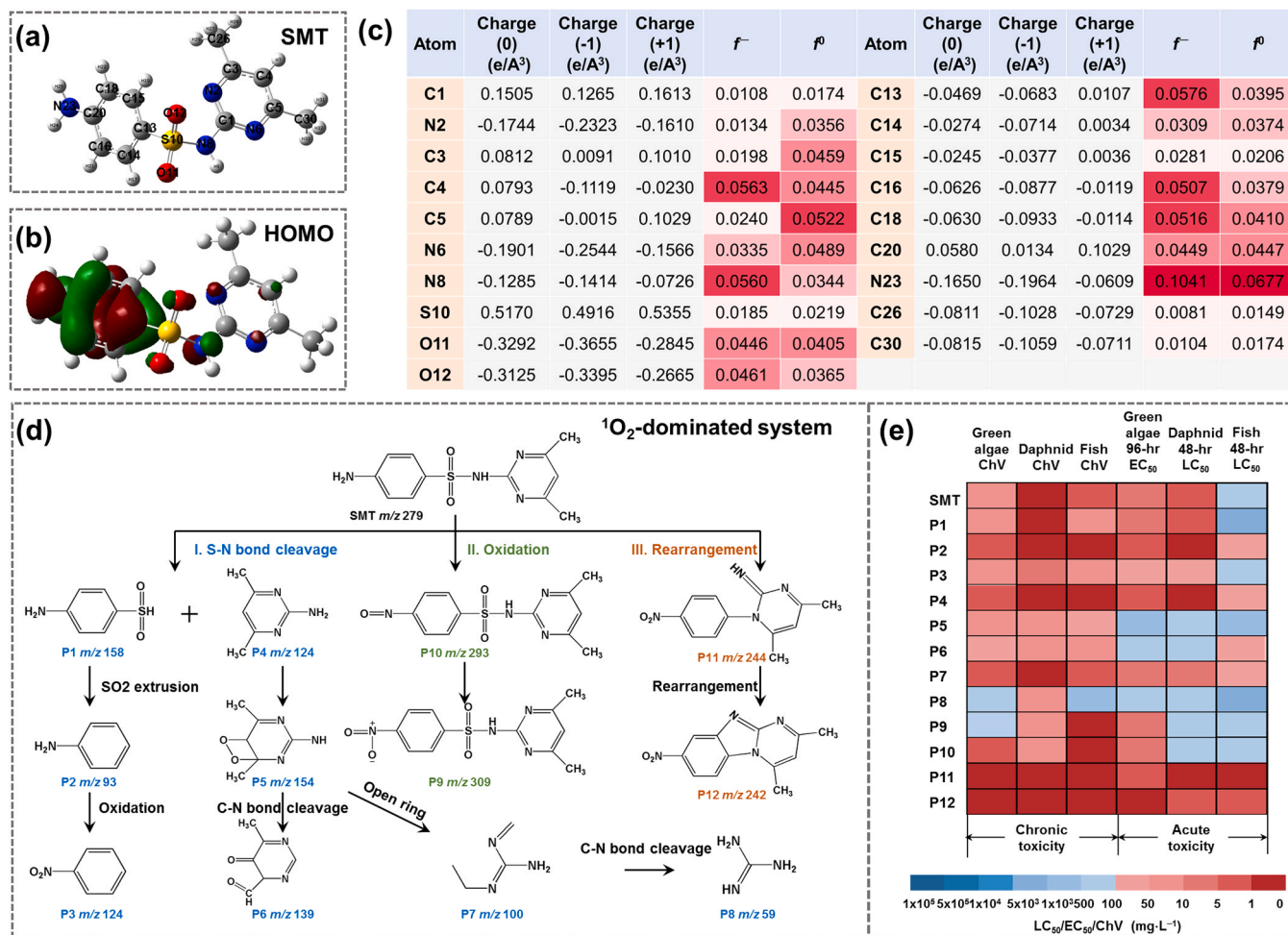


Fig. 7. (a) Chemical structure and (b) HOMO of SMT. (c) SMT charge distributions and f^- . (d) The proposed degradation pathway of SMT in the Co₉S₈-3/PMS system. (e) Toxicity assessment on SMT and its degradation intermediates in the Co₉S₈-3/PMS system.

electron-deficient groups (–NO₂ and –COOH) were evaluated. The results revealed that the pollutants with electron-donating groups could be effectively degraded, with removal efficiencies exceeding 95% within 15 min. However, the removal efficiencies of the pollutants with electron-deficient groups were significantly decreased, reaching only approximately 10% (Figs. 8a and 8b). Some researchers showed that the second-order reaction rate constants of ¹O₂ to phenols and sulfonamides with five-membered rings in sunlit surface water under neutral conditions are very low [69,70], so judging that phenols and sulfonamides with five-membered rings are not sensitive to ¹O₂, which was contrary to the results of high degradation rate constant in this work. This might be due to the effect of the second-order reaction rate constant and ROS concentration on the degradation ability of ROS to pollutants [71]. The steady-state concentration of ¹O₂ ([¹O₂]_{ss}) in the Co₉S₈-3/PMS system was detected through the loss of FFA (Fig. S23), which was detailed in Text S14. The results indicated that the [¹O₂]_{ss} in Co₉S₈-3/PMS system was 4.6 × 10^{−9} M higher than that in the surface water (< 10^{−12} M) [72], resulting in excellent degradation performance of Co₉S₈-3/PMS on SMX, Ph, and BPA, which was consistent with the reported literature results [9, 73,74]. Besides, different degradation performance of these organics might be attributed to their substituents, whose electronic effects had a great influence on the reaction between organic substrate and ¹O₂ [75, 76]. For substituent contrast alone (ANI and Ph), ¹O₂ had a stronger reaction performance toward –NH₂ than did –OH substituents. Furthermore, the reaction rate constants of sulfonamides (SAs) with different substituents were significantly higher than those without substituents. Since aniline is part of the organic moiety of SAs, its higher

reactivity relative to SAs suggests that the aniline moiety, rather than the thiazole and isoxazole ring moieties. Substituents had a different effect on the degradation rate of the sulfonamides, which may be attributed to the fact that the –CH₃ substituents can increase the electron density on the –NH₂ group due to the conjugation of lone pairs on the electron-donating group [77]. Therefore, it was speculated that –NH₂ as an electron donating group might have the highest reaction performance with ¹O₂. DFT calculations were employed to evaluate the nucleophilicity of pollutants except NB and BA to understand the different reactivity of different pollutants in ¹O₂ system. The nucleophilicity index (N index) was usually described by the nucleophilicity with HOMO energy (Table S8) [78]. The good linear between reaction rate and the N index of organic pollutants was obtained (Fig. 8c). In summary, the ¹O₂ system substituents, which might depend on the mutual cooperation of different electron-donating groups and the nucleophilicity of the organics. Finally, a fixed bed reactor was established to immobilize Co₉S₈ on a polyester fiber ball (PFB) carrier and to test its continuous decontamination performance, which was detailed in Text S15. PFB carriers have superior wettability and high porosity, which are conducive to adequate water dispersion [46]. During continuous operation, removal efficiencies of more than 90% (Fig. 8d) were achieved for SMT, suggesting that the catalyst has strong practical application potential. The aforementioned results revealed that the developed Co₉S₈-3 had considerable potential for SA wastewater treatment under complex water matrices.

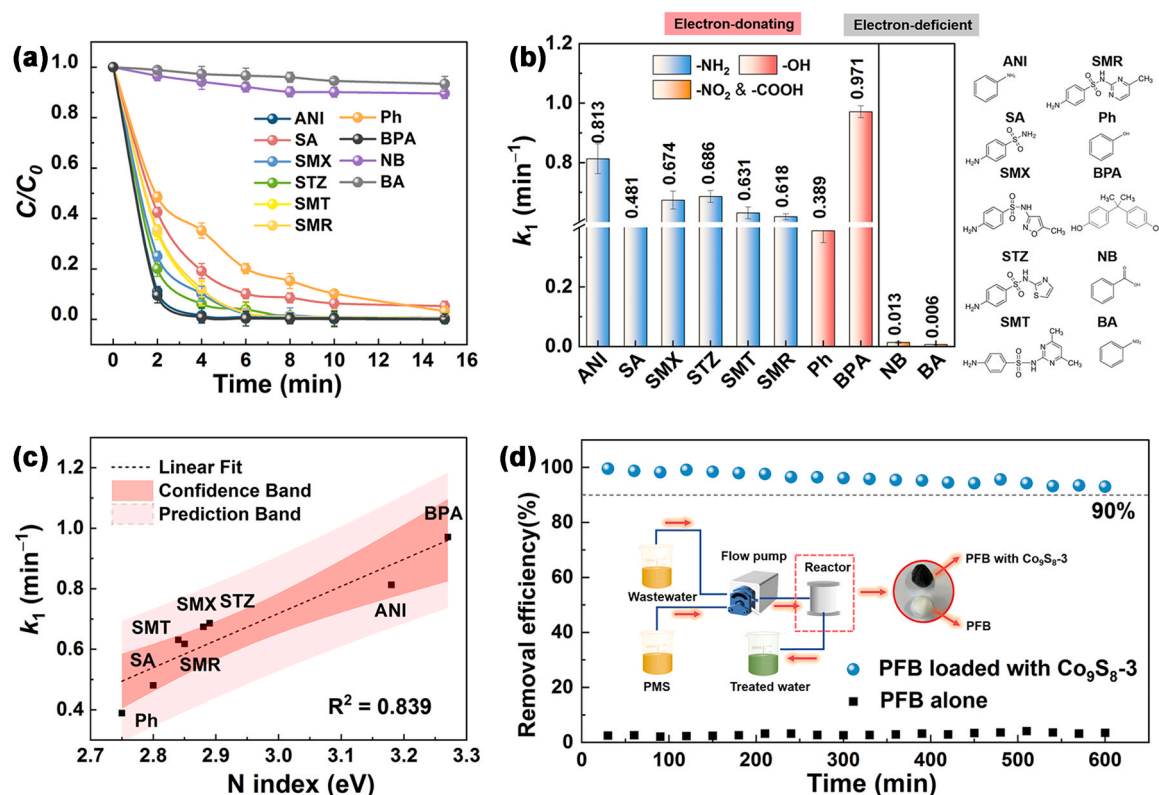


Fig. 8. (a) The degradation curves of different pollutants in Co₉S₈-3/PMS system. (b) k_1 values and structural formula of organics. (c) Correlation between k_1 values and N index. Reaction condition: [catalyst] = 150 mg·L⁻¹, [PMS] = 0.6 mM, [pollutant] = 36.6 μM (The molar concentration is converted according to the 10 mg·L⁻¹ SMT concentration), and initial pH = 6.9 ± 0.2. (d) The removal efficiency of SMT in the fixed bed reactor.

4. Conclusions

In summary, a series of Co₉S₈-X catalysts with tunable V_S by using ZIF-67 as the sacrificial template and controlling the sulfur source dosage were successfully achieved to explore the catalytic selectivity. Among the catalysts, Co₉S₈-3 exhibited unexpected selectivity in the generation of ¹O₂ active species during PMS activation, which facilitated an extremely rapid SMT degradation rate of 0.631 min⁻¹. The V_S /PMS system demonstrated excellent resistance to interference from various environmental factors such as anions, cations, and NOM, and exhibited effective performance over a wide pH range of 5–11. Both experimental results and theoretical calculations revealed that the high PMS activation and selectivity for ¹O₂ generation were associated with the incorporation of V_S , which had lower adsorption energy and smaller reaction energy barrier for O–O bond breaking in HSO₅⁻, which promoted the formation of [•]O, a key precursor of ¹O₂. The study results indicated that the selective degradation of organic pollutants by ¹O₂ depends on the presence of electron-donating groups and the nucleophilicity of the pollutant. The findings provided a basis for the rational design of electronic structures of active sites to selectively produce ¹O₂ and might be used as a reference for future studies on the mechanism underlying ¹O₂ generation at the molecular level.

CRediT authorship contribution statement

Zhimo Fang: Conceptualization, Methodology, Software, Visualization, Writing – original draft. **Juanjuan Qi:** Writing – review & editing, Funding acquisition, Data curation. **Wenxing Chen:** Methodology, Resources, Software. **Lin Zhang:** Software. **Jianhui Wang:** Writing – review & editing. **Caili Tian:** Methodology. **Qin Dai:** Investigation, Methodology. **Wen Liu:** Writing – review & editing, Funding acquisition. **Lidong Wang:** Writing – review & editing, Funding acquisition.

Declaration of Competing Interest

The authors declare that they have no known competing financial interests or personal relationships that could have appeared to influence the work reported in this paper.

Data availability

Data will be made available on request.

Acknowledgements

This work was financially supported by the National Natural Science Foundation of China (No. 51878273, No. 22106045), National Key Research and Development Program of China (No. 2021YFA1202500), the Natural Science Foundation of Hebei Province (No. E2019502199). The authors would like to thank ECOSAR software supplied by the U.S. Environmental Protection Agency.

Appendix A. Supporting information

Supplementary data associated with this article can be found in the online version at [doi:10.1016/j.apcatb.2023.123084](https://doi.org/10.1016/j.apcatb.2023.123084).

References

- [1] T. An, H. Yang, G. Li, W. Song, W.J. Cooper, X. Nie, Kinetics and mechanism of advanced oxidation processes (AOPs) in degradation of ciprofloxacin in water, Appl. Catal. B 94 (2010) 288–294, <https://doi.org/10.1016/j.apcatb.2009.12.002>.
- [2] L. Wu, Z. Sun, Y. Zhen, S. Zhu, C. Yang, J. Lu, Y. Tian, D. Zhong, J. Ma, Oxygen vacancy-induced nonradical degradation of organics: critical trigger of oxygen (¹O₂) in the Fe-Co LDH/peroxymonosulfate system, Environ. Sci. Technol. 55 (2021) 15400–15411, <https://doi.org/10.1021/acs.est.1c04600>.
- [3] P. Yang, Y. Long, W. Huang, D. Liu, Single-atom copper embedded in two-dimensional MXene toward peroxymonosulfate activation to generate singlet

- oxygen with nearly 100% selectivity for enhanced Fenton-like reactions, *Appl. Catal. B* 324 (2023), 122245, <https://doi.org/10.1016/j.apcatb.2022.122245>.
- [4] H. Chen, Y. Xu, K. Zhu, H. Zhang, Understanding oxygen-deficient $\text{La}_2\text{CuO}_{4-x}$ perovskite activated peroxymonosulfate for bisphenol A degradation: the role of localized electron within oxygen vacancy, *Appl. Catal. B* 284 (2021), 119732, <https://doi.org/10.1016/j.apcatb.2020.119732>.
 - [5] Y. Yao, C. Wang, X. Yan, H. Zhang, C. Xiao, J. Qi, Z. Zhu, Y. Zhou, X. Sun, X. Duan, J. Li, Rational regulation of Co-N-C coordination for high-efficiency Generation of $^1\text{O}_2$ toward nearly 100% selective degradation of organic pollutants, *Environ. Sci. Technol.* 56 (2022) 8833–8843, <https://doi.org/10.1021/acs.est.2c00706>.
 - [6] X. Mi, P. Wang, S. Xu, L. Su, H. Zhong, H. Wang, Y. Li, S. Zhan, Almost 100% peroxymonosulfate conversion to singlet oxygen on single-atom CoN_{2+2} sites, *Angew. Chem. Int. Ed.* 60 (2021) 4588–4593, <https://doi.org/10.1002/anie.202014472>.
 - [7] Y. Gao, Z. Chen, Y. Zhu, T. Li, C. Hu, New insights into the generation of singlet oxygen in the metal-free peroxymonosulfate activation process: important role of electron-deficient carbon atoms, *Environ. Sci. Technol.* 54 (2020) 1232–1241, <https://doi.org/10.1021/acs.est.9b05856>.
 - [8] J. Wu, J. Wang, C. Liu, C. Nie, T. Wang, X. Xie, J. Cao, J. Zhou, H. Huang, D. Li, S. Wang, Z. Ao, Removal of gaseous volatile organic compounds by a multiwalled carbon nanotubes/peroxymonosulfate wet scrubber, *Environ. Sci. Technol.* (2022) 13996–14007, <https://doi.org/10.1021/acs.est.2c03590>.
 - [9] L. Xie, P. Wang, Y. Li, D. Zhang, D. Shang, W. Zheng, Y. Xia, S. Zhan, W. Hu, Pauling-type adsorption of O_2 induced electrocatalytic singlet oxygen production on N-CuO for organic pollutants degradation, *Nat. Commun.* 13 (2022) 5560, <https://doi.org/10.1038/s41467-022-33149-4>.
 - [10] L. Yang, H. Yang, S. Yin, X. Wang, M. Xu, G. Lu, Z. Liu, H. Sun, Fe single-atom catalyst for efficient and rapid Fenton-like degradation of organics and disinfection against bacteria, *Small* 18 (2022), 2104941, <https://doi.org/10.1002/sml.202104941>.
 - [11] J. Ji, Q. Yan, P. Yin, S. Mine, M. Matsuoka, M. Xing, Tuning redox reactions via defects on CoS_{2-x} for sustainable degradation of organic pollutants, *Angew. Chem. Int. Ed.* 60 (2021) 2903–2908, <https://doi.org/10.1002/anie.202013015>.
 - [12] F. Wang, H. Fu, F.X. Wang, X.W. Zhang, P. Wang, C. Zhao, C.C. Wang, Enhanced catalytic sulfamethoxazole degradation via peroxymonosulfate activation over amorphous Co_x/SiO_2 nanocages derived from ZIF-67, *J. Hazard. Mater.* 423 (2022), 126998, <https://doi.org/10.1016/j.jhazmat.2021.126998>.
 - [13] Y. Ding, Y. Hu, X. Peng, Y. Xiao, J. Huang, Micro-nano structured CoS: an efficient catalyst for peroxymonosulfate activation for removal of bisphenol A, *Sep. Purif. Technol.* 233 (2020), <https://doi.org/10.1016/j.seppur.2019.116022>.
 - [14] C. Zhu, F. Liu, C. Ling, H. Jiang, H. Wu, A. Li, Growth of graphene-supported hollow cobalt sulfide nanocrystals via MOF-templated ligand exchange as surface-bound radical sinks for highly efficient bisphenol A degradation, *Appl. Catal. B* 242 (2019) 238–248, <https://doi.org/10.1016/j.apcatb.2018.09.088>.
 - [15] Z. Wang, E. Almatrafi, H. Wang, H. Qin, W. Wang, L. Du, S. Chen, G. Zeng, P. Xu, Cobalt single atoms anchored on oxygen-doped tubular carbon nitride for efficient peroxymonosulfate activation: simultaneous coordination structure and morphology modulation, *Angew. Chem. Int. Ed.* 61 (2022), e202202338, <https://doi.org/10.1002/anie.202202338>.
 - [16] X. Zhou, M.K. Ke, G.X. Huang, C. Chen, W. Chen, K. Liang, Y. Qu, J. Yang, Y. Wang, F. Li, H.Q. Yu, Y. Wu, Identification of Fenton-like active Cu sites by heteroatom modulation of electronic density, *Proc. Natl. Acad. Sci. USA*, 119 (2022) e2119492119, <https://doi.org/10.1073/pnas.2119492119>.
 - [17] J. Jiang, Z. Zhao, J. Gao, T. Li, M. Li, D. Zhou, S. Dong, Nitrogen vacancy-modulated peroxymonosulfate nonradical activation for organic contaminant removal via high-valent cobalt-oxo species, *Environ. Sci. Technol.* 56 (2022) 5611–5619, <https://doi.org/10.1021/acs.est.2c01913>.
 - [18] X. Yang, Y. Luo, J. Li, H. Wang, Y. Song, J. Li, Z. Guo, Tuning mixed electronic/ionic conductivity of 2D CdPS_3 nanosheets as an anode material by synergistic intercalation and vacancy engineering, *Adv. Funct. Mater.* 32 (2022), 2112169, <https://doi.org/10.1002/adfm.202112169>.
 - [19] Q. Wang, L. Yan, L. Wang, W. Zhang, Y. Guo, W. Song, X. Li, Enhanced peroxymonosulfate activation by $(\text{NH}_4)_2\text{MoS}_3$ for organic pollutant removal: Crucial roles of adsorption and singlet oxygen, *J. Environ. Chem. Eng.* 10 (2022), 107966, <https://doi.org/10.1016/j.jece.2022.107966>.
 - [20] Y. Gu, T. Gao, F. Zhang, C. Lu, W. Cao, Z. Fu, C. Hu, L. Lyu, Surface sulfur vacancies enhanced electron transfer over Co-ZnS quantum dots for efficient degradation of plasticizer micropollutants by peroxymonosulfate activation, *Chin. Chem. Lett.* 33 (2022) 3829–3834, <https://doi.org/10.1016/j.ccl.2021.12.004>.
 - [21] H. Hu, B. Guan, B. Xia, X.W. Lou, Designed formation of $\text{Co}_3\text{O}_4/\text{NiCo}_2\text{O}_4$ double-shelled nanocages with enhanced pseudocapacitive and electrocatalytic properties, *J. Am. Chem. Soc.* 137 (2015) 5590–5595, <https://doi.org/10.1021/jacs.5b02465>.
 - [22] H. Hu, B. Guan, X. Lou, Construction of complex CoS hollow structures with enhanced electrochemical properties for hybrid supercapacitors, *Chem* 1 (2016) 102–113, <https://doi.org/10.1016/j.chempr.2016.06.001>.
 - [23] Z.F. Huang, J. Song, K. Li, M. Tahir, Y.T. Wang, L. Pan, L. Wang, X. Zhang, J.J. Zou, Hollow cobalt-based bimetallic sulfide polyhedra for efficient all-pH-value electrochemical and photocatalytic hydrogen evolution, *J. Am. Chem. Soc.* 138 (2016) 1359–1365, <https://doi.org/10.1021/jacs.5b11986>.
 - [24] M. Kim, M.A.R. Anjum, M. Choi, H.Y. Jeong, S.H. Choi, N. Park, J.S. Lee, Covalent 0D–2D heterostructuring of Co_9S_8 – MoS_2 for enhanced hydrogen evolution in all pH electrolytes, *Adv. Funct. Mater.* 30 (2020), 2002536, <https://doi.org/10.1002/adfm.202002536>.
 - [25] C. Du, Q. Zhang, Z. Lin, B. Yan, C. Xia, G. Yang, Half-unit-cell ZnIn_2S_4 monolayer with sulfur vacancies for photocatalytic hydrogen evolution, *Appl. Catal. B* 248 (2019) 193–201, <https://doi.org/10.1016/j.apcatb.2019.02.027>.
 - [26] P. Gao, Z. Chen, Y. Gong, R. Zhang, H. Liu, P. Tang, X. Chen, S. Passerini, J. Liu, The role of cation vacancies in electrode materials for enhanced electrochemical energy storage: Synthesis, advanced characterization, and fundamentals, *Adv. Energy Mater.* 10 (2020), 1903780, <https://doi.org/10.1002/aenm.201903780>.
 - [27] J. Zhou, J. Zhao, R. Liu, Defect engineering of zeolite imidazole framework derived ZnS nanosheets towards enhanced visible light driven photocatalytic hydrogen production, *Appl. Catal. B* 278 (2020), 119265, <https://doi.org/10.1016/j.apcatb.2020.119265>.
 - [28] F. Chen, Z. Zhang, W. Liang, X. Qin, Z. Zhang, L. Jiang, Synthesis of $\text{Co}_4\text{S}_3/\text{Co}_9\text{S}_8$ nanosheets and comparison study toward the OER properties induced by different metal ion doping, *Chin. Chem. Lett.* 33 (2022) 1395–1402, <https://doi.org/10.1016/j.ccl.2021.08.019>.
 - [29] Y. Li, T. Chen, S. Zhao, P. Wu, Y. Chong, A. Li, Y. Zhao, G. Chen, X. Jin, Y. Qiu, D. Ye, Engineering cobalt oxide with coexisting cobalt defects and oxygen vacancies for enhanced catalytic oxidation of toluene, *ACS Catal.* 12 (2022) 4906–4917, <https://doi.org/10.1021/acscatal.2c00296>.
 - [30] Y. Shen, J. Deng, S. Impeng, S. Li, T. Yan, J. Zhang, L. Shi, D. Zhang, Boosting toluene combustion by engineering Co-O strength in cobalt oxide catalysts, *Environ. Sci. Technol.* 54 (2020) 10342–10350, <https://doi.org/10.1021/acs.est.0c02680>.
 - [31] C. Zhang, Y. Shi, Y. Yu, Y. Du, B. Zhang, Engineering sulfur defects, atomic thickness, and porous structures into cobalt sulfide nanosheets for efficient electrocatalytic alkaline hydrogen evolution, *ACS Catal.* 8 (2018) 8077–8083, <https://doi.org/10.1021/acscatal.8b02056>.
 - [32] B. Qiu, Q. Zhu, M. Du, L. Fan, M. Xing, J. Zhang, Efficient solar light harvesting $\text{CdS}/\text{Co}_9\text{S}_8$ hollow cubes for Z-scheme photocatalytic water splitting, *Angew. Chem. Int. Ed.* 56 (2017) 2684–2688, <https://doi.org/10.1002/anie.201612551>.
 - [33] H. Xu, J. Cao, C. Shan, B. Wang, P. Xi, W. Liu, Y. Tang, MOF-derived hollow CoS decorated with CeOx nanoparticles for boosting oxygen evolution reaction electrocatalysis, *Angew. Chem. Int. Ed.* 57 (2018) 8654–8658, <https://doi.org/10.1002/anie.201804673>.
 - [34] Z. Ye, Y. Jiang, L. Li, F. Wu, R. Chen, Synergetic anion vacancies and dense heterointerfaces into bimetal chalcogenide nanosheet arrays for boosting electrocatalysis sulfur conversion, *Adv. Mater.* 34 (2022), e2109552, <https://doi.org/10.1002/adma.202109552>.
 - [35] X. Liu, L. Zhao, H. Xu, Q. Huang, Y. Wang, C. Hou, Y. Hou, J. Wang, F. Dang, J. Zhang, Tunable cationic vacancies of cobalt oxides for efficient electrocatalysis in Li-O_2 batteries, *Adv. Energy Mater.* 10 (2020), 2001415, <https://doi.org/10.1002/aenm.202001415>.
 - [36] J. Lee, S. Ham, D. Choi, D.J. Jang, Facile fabrication of porous ZnS nanostructures with a controlled amount of S vacancies for enhanced photocatalytic performances, *Nanoscale* 10 (2018) 14254–14263, <https://doi.org/10.1039/c8nr02936a>.
 - [37] X. Bai, X. Wang, T. Jia, L. Guo, D. Hao, Z. Zhang, L. Wu, X. Zhang, H. Yang, Y. Gong, J. Li, H. Li, Efficient degradation of PPCPs by $\text{Mo}_{1-x}\text{S}_{2-y}$ with S vacancy at phase-junction: promoted by innergenerate- H_2O_2 , *Appl. Catal. B* 310 (2022), 121302, <https://doi.org/10.1016/j.apcatb.2022.121302>.
 - [38] N. Li, R. Li, X. Duan, B. Yan, W. Liu, Z. Cheng, G. Chen, L. Hou, S. Wang, Correlation of active sites to generated reactive species and degradation routes of organics in peroxymonosulfate activation by co-loaded carbon, *Environ. Sci. Technol.* 55 (2021) 16163–16174, <https://doi.org/10.1021/acs.est.1c06244>.
 - [39] T.X. Wang, D.W. Margerum, Kinetics of reversible chlorine hydrolysis: temperature dependence and general-acid/base-assisted mechanisms, *Inorg. Chem.* 33 (1994) 1050–1055, <https://doi.org/10.1021/ic00084a014>.
 - [40] Jz.Kr Gabor Lente, Zsuzsa Baranyai, Aliz Kun, IldikoKek, David Bajusz, Marcell Takacs, Lilla Veres, and Istvan Fabian, One-Versus two-electron oxidation with peroxymonosulfate ion: Reactions with Iron(II), Vanadium(IV), Halide Ions, and photoreaction with Cerium(III), *Inorg. Chem.*, 48 (2009) 1763–1773. (<https://doi.org/10.1021/ic801569k>).
 - [41] A. Wang, B.Z. Zhu, C.H. Huang, W.X. Zhang, M. Wang, X. Li, L. Ling, J. Ma, J. Fang, Generation mechanism of singlet oxygen from the interaction of peroxymonosulfate and chloride in aqueous systems, *Water Res.* 235 (2023), 119904, <https://doi.org/10.1016/j.watres.2023.119904>.
 - [42] Y. Jiang, R. Raliya, P. Liao, P. Biswas, J.D. Fortner, Graphene oxides in water: assessing stability as a function of material and natural organic matter properties, *Environ. Sci. Nano* 4 (2017) 1484–1493, <https://doi.org/10.1039/c7en00220c>.
 - [43] P. Duan, Y. Qi, S. Feng, X. Peng, W. Wang, Y. Yue, Y. Shang, Y. Li, B. Gao, X. Xu, Enhanced degradation of clothianidin in peroxymonosulfate/catalyst system via core-shell FeMn@N-C and phosphate surrounding, *Appl. Catal. B* 267 (2020), 118717, <https://doi.org/10.1016/j.apcatb.2020.118717>.
 - [44] J. Qi, X. Yang, P.-Y. Pan, T. Huang, X. Yang, C.-C. Wang, W. Liu, Interface Engineering of Co(OH)_2 nanosheets growing on the KNO_3 perovskite based on electronic structure modulation for enhanced peroxymonosulfate activation, *Environ. Sci. Technol.* 56 (2022) 5200–5212, <https://doi.org/10.1021/acs.est.1c08806>.
 - [45] Y. Bao, C. Lian, K. Huang, H. Yu, W. Liu, J. Zhang, M. Xing, Generating high-valent iron-oxo identical with Fe(IV)=O complexes in neutral microenvironments through peroxymonosulfate activation by Zn-Fe layered double hydroxides, *Angew. Chem. Int. Ed.* (2022), e202209542, <https://doi.org/10.1002/anie.202209542>.
 - [46] Z.Y. Guo, Y. Si, W.Q. Xia, F. Wang, H.Q. Liu, C. Yang, W.J. Zhang, W.W. Li, Electron delocalization triggers nonradical Fenton-like catalysis over spinel oxides, *Proc. Natl. Acad. Sci., USA*, 119 (2022) e2201607119, (<https://doi.org/10.1073/pnas.2201607119>).
 - [47] X. Liu, Z. Hao, H. Wang, T. Wang, Z. Shen, H. Zhang, S. Zhan, J. Gong, Enhanced localized dipole of Pt-Au single-site catalyst for solar water splitting, *Proc. Natl. Acad. Sci. USA*, 119 (2022) e2119723119, (<https://doi.org/10.1073/pnas.2119723119>).

- [48] S. Yin, X. Zhao, E. Jiang, Y. Yan, P. Zhou, P. Huo, Boosting water decomposition by sulfur vacancies for efficient CO₂ photoreduction, *Energy Environ. Sci.* 15 (2022) 1556–1562, <https://doi.org/10.1039/d1ee03764a>.
- [49] R. Zhang, Y.-C. Zhang, L. Pan, G.-Q. Shen, N. Mahmood, Y.-H. Ma, Y. Shi, W. Jia, L. Wang, X. Zhang, W. Xu, J.-J. Zou, Engineering cobalt defects in cobalt oxide for highly efficient electrocatalytic oxygen evolution, *ACS Catal.* 8 (2018) 3803–3811, <https://doi.org/10.1021/acscatal.8b01046>.
- [50] R. Guo, Y. Wang, J. Li, X. Cheng, D.D. Dionysiou, Sulfamethoxazole degradation by visible light assisted peroxymonosulfate process based on nanohybrid manganese dioxide incorporating ferric oxide, *Appl. Catal. B* 278 (2020), 119297, <https://doi.org/10.1016/j.apcatb.2020.119297>.
- [51] J. Liang, L. Fu, K. Gao, X. Duan, Accelerating radical generation from peroxymonosulfate by confined variable Co species toward ciprofloxacin mineralization: ROS quantification and mechanisms elucidation, *Appl. Catal. B* 315 (2022), 121542, <https://doi.org/10.1016/j.apcatb.2022.121542>.
- [52] L. Wu, B. Li, Y. Li, X. Fan, F. Zhang, G. Zhang, Q. Xia, W. Peng, Preferential growth of the cobalt (200) facet in Co@N-C for enhanced performance in a Fenton-like reaction, *ACS Catal.* 11 (2021) 5532–5543, <https://doi.org/10.1021/acscatal.1c00701>.
- [53] J. Lee, U. von Gunten, J.H. Kim, Persulfate-based advanced oxidation: critical assessment of opportunities and roadblocks, *Environ. Sci. Technol.* 54 (2020) 3064–3081, <https://doi.org/10.1021/acs.est.9b07082>.
- [54] X. Li, J. Wang, X. Duan, Y. Li, X. Fan, G. Zhang, F. Zhang, W. Peng, Fine-tuning radical/nonradical pathways on graphene by porous engineering and doping strategies, *ACS Catal.* 11 (2021) 4848–4861, <https://doi.org/10.1021/acscatal.0c05089>.
- [55] S. Lan, C. Yu, E. Wu, M. Zhu, D.D. Dionysiou, Self-powered water flow-triggered piezocatalytic generation of reactive oxygen species for water purification in simulated water drainage, *ACS EST Eng.* 2 (2021) 101–109, <https://doi.org/10.1021/acsestengg.1c00296>.
- [56] R. Hao, W. Sun, Q. Liu, X. Liu, J. Chen, X. Lv, W. Li, Y.P. Liu, Z. Shen, Efficient electrochemical nitrogen fixation over isolated Pt sites, *Small* 16 (2020), e2000015, <https://doi.org/10.1002/sml.202000015>.
- [57] P. Zhang, Y. Yang, X. Duan, Y. Liu, S. Wang, Density functional theory calculations for insight into the heterocatalyst reactivity and mechanism in persulfate-based advanced oxidation reactions, *ACS Catal.* 11 (2021) 11129–11159, <https://doi.org/10.1021/acscatal.1c03099>.
- [58] J. Li, M. Li, H. Sun, Z. Ao, S. Wang, S. Liu, Understanding of the oxidation behavior of benzyl alcohol by peroxymonosulfate via carbon nanotubes activation, *ACS Catal.* 10 (2020) 3516–3525, <https://doi.org/10.1021/acscatal.9b05273>.
- [59] X. Xu, Y. Zhang, Y. Chen, C. Liu, W. Wang, J. Wang, H. Huang, J. Feng, Z. Li, Z. Zou, Revealing *OOH key intermediates and regulating H₂O₂ photoactivation by surface relaxation of Fenton-like catalysts, *Proc. Natl. Acad. Sci. USA* 119 (2022), e2205562119, <https://doi.org/10.1073/pnas.2205562119>.
- [60] S. Chen, Z. Zhang, W. Jiang, S. Zhang, J. Zhu, L. Wang, H. Ou, S. Zaman, L. Tan, P. Zhu, E. Zhang, P. Jiang, Y. Su, D. Wang, Y. Li, Engineering water molecules activation center on multisite electrocatalysts for enhanced CO₂ methanation, *J. Am. Chem. Soc.* 144 (2022) 12807–12815, <https://doi.org/10.1021/jacs.2c03875>.
- [61] T. Lu, F. Chen, Multiwfn: a multifunctional wavefunction analyzer, *J. Comput. Chem.* 33 (2012) 580–592, <https://doi.org/10.1002/jcc.22885>.
- [62] C. Zhang, S. Tian, F. Qin, Y. Yu, D. Huang, A. Duan, C. Zhou, Y. Yang, W. Wang, Y. Zhou, H. Luo, Catalyst-free activation of permanganate under visible light irradiation for sulfamethazine degradation: experiments and theoretical calculation, *Water Res.* 194 (2021), 116915, <https://doi.org/10.1016/j.watres.2021.116915>.
- [63] Y. Li, H. Dong, L. Li, J. Xiao, S. Xiao, Z. Jin, Efficient degradation of sulfamethazine via activation of percarbonate by chalcopyrite, *Water Res.* 202 (2021), 117451, <https://doi.org/10.1016/j.watres.2021.117451>.
- [64] L. Wang, K. Xiao, H. Zhao, The debatable role of singlet oxygen in persulfate-based advanced oxidation processes, *Water Res.* 235 (2023), 119925, <https://doi.org/10.1016/j.watres.2023.119925>.
- [65] J. Al-Nu'airat, I. Oluwoye, N. Zeinali, M. Altarawneh, B.Z. Dlugogorski, Review of chemical reactivity of singlet oxygen with organic fuels and contaminants, *Chem. Rec.* 21 (2021) 315–342, <https://doi.org/10.1002/tcr.202000143>.
- [66] R. Yin, W. Guo, H. Wang, J. Du, Q. Wu, J.-S. Chang, N. Ren, Singlet oxygen-dominated peroxydisulfate activation by sludge-derived biochar for sulfamethoxazole degradation through a nonradical oxidation pathway: performance and mechanism, *Chem. Eng. J.* 357 (2019) 589–599, <https://doi.org/10.1016/j.cej.2018.09.184>.
- [67] R. Yin, W. Guo, N. Ren, L. Zeng, M. Zhu, New insight into the substituents affecting the peroxydisulfate nonradical oxidation of sulfonamides in water, *Water Res.* 171 (2020), 115374, <https://doi.org/10.1016/j.watres.2019.115374>.
- [68] X. Nie, G. Li, S. Li, Y. Luo, W. Luo, Q. Wan, T. An, Highly efficient adsorption and catalytic degradation of ciprofloxacin by a novel heterogeneous Fenton catalyst of hexapod-like pyrite nanosheets mineral clusters, *Appl. Catal. B* 300 (2022), 120734, <https://doi.org/10.1016/j.apcatb.2021.120734>.
- [69] P.G.Ta.J. Hoigné, Oxidation of substituted phenols in the environment: a QSAR analysis of rate constants for reaction with singlet oxygen, *Environ. Sci. Technol.* 25 (1991) 1596–1604, <https://doi.org/10.1021/es00021a011>.
- [70] W.A.A. Anne L. Boreen, Kristopher Mcneill, Photochemical fate of sulfa drugs in the aquatic environment: sulfa drugs containing five-membered heterocyclic groups, *Environ. Sci. Technol.* 38 (2004) 3933–3940, <https://doi.org/10.1021/es0353053>.
- [71] Z.H. Xie, C.S. He, H.Y. Zhou, L.L. Li, Y. Liu, Y. Du, W. Liu, Y. Mu, B. Lai, Effects of molecular structure on organic contaminants' degradation efficiency and dominant ROS in the advanced oxidation process with multiple ROS, *Environ. Sci. Technol.* 56 (2022) 8784–8795, <https://doi.org/10.1021/acs.est.2c00464>.
- [72] W.R.Ha.J. Hoigné, Singlet oxygen in surface waters. 3. Photochemical formation and steady-state concentrations in various types of waters, *Environ. Sci. Technol.* 20 (1986) 341–348, <https://doi.org/10.1021/es00146a005>.
- [73] Z. Yang, J. Qian, A. Yu, B. Pan, Singlet oxygen mediated iron-based Fenton-like catalysis under nanoconfinement, *Proc. Natl. Acad. Sci. USA*, 116 (2019) 6659–6664, <https://doi.org/10.1073/pnas.1819382116>.
- [74] J. You, C. Zhang, Z. Wu, Z. Ao, W. Sun, Z. Xiong, S. Su, G. Yao, B. Lai, N-doped graphite encapsulated metal nanoparticles catalyst for removal of Bisphenol A via activation of peroxymonosulfate: a singlet oxygen-dominated oxidation process, *Chem. Eng. J.* 415 (2021), 128890, <https://doi.org/10.1016/j.cej.2021.128890>.
- [75] M. Huang, Y. Han, W. Xiang, D. Zhong, C. Wang, T. Zhou, X. Wu, J. Mao, In situ-formed phenoxyl radical on the CuO surface triggers efficient persulfate activation for phenol degradation, *Environ. Sci. Technol.* 55 (2021) 15361–15370, <https://doi.org/10.1021/acs.est.1c03758>.
- [76] Y. Zhao, L. Yu, C. Song, Z. Chen, F. Meng, M. Song, Selective degradation of electron-rich organic pollutants induced by CuO@biochar: the key role of outer-sphere interaction and singlet oxygen, *Environ. Sci. Technol.* 56 (2022) 10710–10720, <https://doi.org/10.1021/acs.est.2c01759>.
- [77] T. Liu, J. Chen, N. Li, S. Xiao, C.H. Huang, L. Zhang, Y. Xu, Y. Zhang, X. Zhou, Unexpected role of nitrite in promoting transformation of sulfonamide antibiotics by peracetic acid: reactive nitrogen species contribution and harmful disinfection byproduct formation potential, *Environ. Sci. Technol.* 56 (2022) 1300–1309, <https://doi.org/10.1021/acs.est.1c06026>.
- [78] K. Zhang, X. Zhou, P. Du, T. Zhang, M. Cai, P. Sun, C.H. Huang, Oxidation of beta-lactam antibiotics by peracetic acid: reaction kinetics, product and pathway evaluation, *Water Res.* 123 (2017) 153–161, <https://doi.org/10.1016/j.watres.2017.06.057>.